

Observations and modelling of the global distribution and long-term trend of atmospheric $^{14}\text{CO}_2$

By INGEBOURG LEVIN^{1,*},†, TOBIAS NAEGLER^{1,†}, BERND KROMER^{1,2}, MORITZ DIEHL^{3,‡}, ROGER J. FRANCEY⁴, ANGEL J. GOMEZ-PELAEZ⁵, L. PAUL STEELE⁴, DIETMAR WAGENBACH¹, ROLF WELLER⁶ and DOUGLAS E. WORTHY⁷ ¹*Institut für Umweltphysik, University of Heidelberg, INF 229, D-69120 Heidelberg, Germany;* ²*Heidelberger Akademie der Wissenschaften, INF 229, D-69120 Heidelberg, Germany;* ³*Interdisziplinäres Zentrum für wissenschaftliches Rechnen (IWR), University of Heidelberg, INF 368, D-69120 Heidelberg, Germany;* ⁴*Centre for Australian Weather and Climate Research / CSIRO Marine and Atmospheric Research (CMAR), Private Bag No. 1, Aspendale, Victoria 3195, Australia;* ⁵*Izaña Atmospheric Research Center, Meteorological State Agency of Spain (AEMET), C/ La Marina, 20, Planta 6, 38071 Santa Cruz de Tenerife, Spain;* ⁶*Alfred Wegener Institute for Polar and Marine Research, Am Handelshafen 12, D-27568 Bremerhaven, Germany;* ⁷*Environment Canada, Climate Research Division / CCMR, 4905 Dufferin St., Toronto, ON M3H 5T4, Canada;*

(Manuscript received 21 May 2009; in final form 9 October 2009)

ABSTRACT

Global high-precision atmospheric $\Delta^{14}\text{CO}_2$ records covering the last two decades are presented, and evaluated in terms of changing (radio)carbon sources and sinks, using the coarse-grid carbon cycle model GRACE. Dedicated simulations of global trends and interhemispheric differences with respect to atmospheric CO_2 as well as $\delta^{13}\text{CO}_2$ and $\Delta^{14}\text{CO}_2$, are shown to be in good agreement with the available observations (1940–2008). While until the 1990s the decreasing trend of $\Delta^{14}\text{CO}_2$ was governed by equilibration of the atmospheric bomb ^{14}C perturbation with the oceans and terrestrial biosphere, the largest perturbation today are emissions of ^{14}C -free fossil fuel CO_2 . This source presently depletes global atmospheric $\Delta^{14}\text{CO}_2$ by 12–14‰ yr^{-1} , which is partially compensated by $^{14}\text{CO}_2$ release from the biosphere, industrial ^{14}C emissions and natural ^{14}C production. Fossil fuel emissions also drive the changing north–south gradient, showing lower $\Delta^{14}\text{C}$ in the northern hemisphere only since 2002. The fossil fuel-induced north–south (and also troposphere–stratosphere) $\Delta^{14}\text{CO}_2$ gradient today also drives the tropospheric $\Delta^{14}\text{CO}_2$ seasonality through variations of air mass exchange between these atmospheric compartments. Neither the observed temporal trend nor the $\Delta^{14}\text{CO}_2$ north–south gradient may constrain global fossil fuel CO_2 emissions to better than 25%, due to large uncertainties in other components of the (radio)carbon cycle.

1. Introduction

The abundance of atmospheric CO_2 is eventually controlled by exchange with the organic and inorganic carbon reservoirs on Earth. Here, the ocean constitutes the most important long-term carbon reservoir with the largest storage capacity for anthropogenic CO_2 , whereas the capacity of the terrestrial biosphere is much smaller and works on much shorter time scales (i.e.

decades to centuries). Any prediction of the future atmospheric CO_2 burden in view of increasing anthropogenic emissions thus strongly relies on a quantitative understanding of the exchange processes between the atmosphere and these carbon compartments (Cox et al., 2000; Friedlingstein et al., 2003; Denman et al., 2007).

Radiocarbon (^{14}C) plays a crucial role in global carbon cycle investigations: Besides using ^{14}C as a dating tool for organic material (Libby, 1961; Stuiver and Reimer, 1993), or to study internal mixing processes of the world oceans (Oeschger et al., 1975; Siegenthaler et al., 1980; Toggweiler et al., 1989), the anthropogenic ^{14}C disturbance through atmospheric nuclear bomb tests (mainly in the 1950s and 1960s) provides an invaluable tracer to gain insight into the carbon cycle dynamics on the decadal time scale (e.g. Levin and Hesshaimer, 2000 and references therein).

*Corresponding author.

e-mail: Ingeborg.Levin@iup.uni-heidelberg.de

†Joint first authors

‡Now at: Electrical Engineering Department (ESAT) and OPTEC, K.U. Leuven, Kasteelpark Arenberg 10, 3001 Leuven, Belgium.

DOI: 10.1111/j.1600-0889.2009.00446.x

Bomb ^{14}C production caused almost a doubling of the $^{14}\text{C}/\text{C}$ ratio in atmospheric CO_2 , leading to a substantial disequilibrium of $^{14}\text{CO}_2$ between atmosphere, biosphere and surface ocean. In the decade following the start of the atmospheric nuclear tests, large observational programs were conducted by a number of laboratories all over the globe to document these disturbances in the stratosphere (Telegadas, 1971), the troposphere (e.g. Nydal and Lövseth, 1983; Levin et al., 1985, 1987, 1992; Manning et al., 1990; Meijer et al., 1995; Rozanski et al., 1995; Levin and Kromer, 1997, 2004; Vogel et al., 2002; Hua and Barbetti, 2004) and the ocean (Broecker et al., 1985; Key et al., 2004). The pre-industrial and pre-bomb ^{14}C level of the last centuries, as monitored by ^{14}C tree-ring analyses from a number of locations in both hemispheres (Stuiver and Quay, 1981; Vogel et al., 1993; Stuiver and Braziunas, 1998; McCormac et al., 2002; Reimer et al., 2004) showed much smaller temporal variations. These were mainly due to changes in natural ^{14}C production (Damon and Sternberg, 1989) and, within the industrial era, by the input of ^{14}C -free fossil fuel CO_2 into the atmosphere (Suess, 1955).

These $\Delta^{14}\text{CO}_2$ observations comprised of all major carbon reservoirs have provided important constraints on global CO_2 exchange fluxes. They have, however, primarily been used to investigate specific aspects of the global carbon cycle, such as studies on air–sea gas exchange (Wanninkhof, 1992; Krakauer et al., 2006; Naegler et al., 2006; Sweeney et al., 2007; Müller et al., 2008; Naegler, 2009), internal mixing of the world oceans (Maier-Reimer and Hasselmann, 1987; Duffy et al., 1995; Rodgers et al., 1997) and on the biospheric carbon turnover on the local (Dörr and Münnich, 1986; Trumbore, 1993; 2000; 2009; Gaudinski et al., 2000) but also on the global scale (Goudriaan, 1992; Naegler and Levin, 2009b).

Global CO_2 exchange fluxes between the atmosphere and the main carbon reservoirs are typically derived from atmospheric CO_2 distribution in combination with inverse modelling (Rayner et al., 1999; Bousquet et al., 2000; Gurney et al., 2002; Rödenbeck et al., 2003). $\delta^{13}\text{CO}_2$ (and $\delta\text{O}_2/\text{N}_2$) observations have also been successfully included in these studies as important constraints distinguishing oceanic and biospheric source/sink contributions (Ciais et al., 1995; Francey et al., 1995; Keeling et al., 1995; Battle et al., 2000; Manning and Keeling, 2006; Rayner et al., 2008). Most attempts towards an integrated understanding of the global carbon cycle including $\Delta^{14}\text{CO}_2$ (and in some cases $\delta^{13}\text{CO}_2$) have been conducted using simple box models (Oeschger et al., 1975; Enting, 1982; Broecker and Peng, 1994; Siegenthaler and Joos, 1992; Heshshaimer et al., 1994; Jain et al., 1996; Lassey et al., 1996; Joos and Bruno, 1998; Naegler and Levin, 2006). However, because most of these models were globally aggregated, they were not capable of simulating north–south differences of both the CO_2 mixing ratio and the isotopic composition of atmospheric CO_2 . Furthermore, because the uncertainty of the global bomb ^{14}C production estimates were large prior to the assessment by Heshshaimer et al. (1994), many studies did not simulate atmospheric $\Delta^{14}\text{C}$ over the period from

pre-bomb time to present. In studies that employed 3-D atmospheric transport models, radiocarbon was primarily used to constrain stratosphere–troposphere exchange (STE, e.g. Johnston, 1989; Kjellström et al., 2000; Land et al., 2002) or assess the possibility of estimating the fossil fuel CO_2 fraction by atmospheric $^{14}\text{CO}_2$ measurements (Levin and Karstens, 2007; Turnbull et al., 2009). Only Braziunas et al. (1995) attempted to simulate the pre-industrial atmospheric $\Delta^{14}\text{CO}_2$ latitudinal gradient. In addition Randerson et al. (2002) also investigated the seasonal and latitudinal variation of $\Delta^{14}\text{CO}_2$ in the atmosphere in the post-bomb era from the 1960s to the 1990s. However, neither of these two studies focussed on an integrated understanding of the temporal (long-term and seasonal) and spatial variability of atmospheric CO_2 mixing ratio as well as $\delta^{13}\text{CO}_2$ and $\Delta^{14}\text{CO}_2$ over the past half century.

One of the main purposes of this paper is to present and make available to the scientific community our complete high-precision global atmospheric $\Delta^{14}\text{CO}_2$ data set covering the past two decades. Using this data, along with earlier published measurements, we will address the following questions:

(1) Is it possible to consistently simulate the atmospheric CO_2 mixing ratio as well as its carbon isotopic composition at globally distributed background monitoring sites from pre-bomb times to the present (i.e. based on published estimates of the global carbon sources and sinks)? For this exercise we use the Global RadioCarbon Exploration model GRACE. If the atmospheric CO_2 , $\delta^{13}\text{CO}_2$ and $\Delta^{14}\text{CO}_2$ can be simulated consistently, we can then safely assume that the underlying carbon fluxes within the atmosphere and between atmosphere and ocean and biosphere are correct.

(2) What are the main drivers of the observed $\Delta^{14}\text{CO}_2$ variability, particularly in the last two decades, and which constraints may be drawn from these features on global carbon fluxes? Using the GRACE simulations, this question is addressed by quantitatively investigating the main components of (i) the long-term trend of atmospheric $\Delta^{14}\text{CO}_2$ and its interannual variation, (ii) the components driving the interhemispheric $\Delta^{14}\text{CO}_2$ gradient and its temporal changes as well as (iii) the components driving the seasonal $\Delta^{14}\text{CO}_2$ variability.

The GRACE model has been previously applied to determine the production of bomb radiocarbon during atmospheric nuclear weapon tests and to quantify the subsequent partitioning of excess radiocarbon among the main carbon reservoirs (Naegler and Levin, 2006). Here we use an updated and improved version of GRACE that also takes into account the spatial and temporal variation of CO_2 and $\delta^{13}\text{CO}_2$. This provided improved and more consistent simulations of all source-sink components of the global carbon cycle through the era of major anthropogenic disturbances (1940–present).

The paper is structured as follows. In Section 2, we first provide a short description of the Heidelberg $^{14}\text{CO}_2$ observational network as well as on our sampling and analysis techniques,

followed by a brief introduction into the GRACE model, and how the different components contributing to trend, north–south gradient and seasonal cycle features have been calculated from the GRACE simulations. A fully detailed description of the model, validation of transport parameters as well as the boundary conditions respectively the $^{14}\text{CO}_2$ exchange fluxes can be found in the Supplementary Information. Section 3 presents the new Heidelberg observational data set and qualitatively describes its main features. Section 4 compares the observations with the GRACE model results, and analyses of the main drivers behind the observed variability. In this section, we also compare our model simulations with earlier estimates made by Rander-son et al. (2002) on the north–south gradient as well as on the seasonal cycle of $\Delta^{14}\text{CO}_2$ and investigate the uncertainties of the component analysis. We then discuss possible constraints of $\Delta^{14}\text{CO}_2$ observations on atmospheric carbon fluxes in the last two decades. Section 5 summarizes our findings and provides a short perspective for future work.

2. Methods

2.1. Sampling sites and experimental techniques

At all stations in the Heidelberg sampling network (see Table 1 and Fig. 1), one- or two-weekly integrated CO_2 samples were collected for ^{14}C analysis from 15 to 25 m^3 of air by chemical absorption in basic solution (NaOH) (Levin et al., 1980). At stations with potential local contamination by fossil CO_2 emissions, sampling was restricted to clean air conditions using local wind direction and speed (Macquarie Island and Mace Head) and continuous aerosol monitoring (Neumayer). Samples were analysed for ^{14}C activity by conventional radioactive counting (Kromer and Münnich, 1992). $\Delta^{14}\text{C}$ was calculated according to Stuiver and Polach (1977, compare eq. (1), corrected for decay), using $\delta^{13}\text{C}$ values analysed by mass spectrometry on the same samples. The precision of individual data, except for the early measurements from Vermunt, was generally $\Delta^{14}\text{C} = \pm 2$ to $\pm 4\%$ (1σ) for samples analysed before 2000 and $\pm 2\%$ or better later on. The improvement of measurement precision was primarily achieved by reducing the natural background activity in the Heidelberg counting laboratory, by increasing sample volume, and by considerably extending counting times. Obvious outliers in the data sets were removed at each station (less than 1% of the data) before calculation of trends and/or seasonal cycles.

2.2. Model set-up

The description of the structure and the validation procedures of the GRACE model used in the present study is presented in detail in the Supplementary Information. Here we only give a short overview of its main characteristics. GRACE is a simple box model of the global carbon (isotopes) cycle, i.e. it calculates

Table 1. Characteristics of $^{14}\text{CO}_2$ station records

Station	Latitude	Longitude	Altitude (m.a.s.l.)	Station type	Period of data availability
ALT: Alert (Canada)	82°27'N	62°31'W	50	GAW Arctic background	Nov 1987–Mar 2008
MHD: Mace Head (Ireland)	53°20'N	9°54'W	25	GAW North Atlantic (marine sector)	Oct 2000–Nov 2007
VER: Vermunt (Austria)	47°04'N	9°34'E	1800	continental European background	Feb 1959–Aug 1986
JFJ: Jungfraujoch (Switzerland)	46°33'N	7°59'E	3450	GAW Continental European background	Aug 1986–Dec 2008
IZA: Izaña (Tenerife, Spain)	28°18'N	16°29'W	2400	GAW marine background	Aug 1984–Mar 2002
MER: Mérida Observatory (Venezuela)	8°47'N	70°52'W	3600	Continental background (night time sampling only)	Apr 1991–Nov 1997
CGO: Cape Grim (Tasmania, Australia)	40°41'S	144°41'E	104	GAW marine background	Apr 1987–Dec 2006
MCQ: Macquarie Island (Australia)	54°30'S	158°56'E	20	Marine background	Dec 1992–Feb 2004
GVN: Neumayer (Antarctica)	70°39'S	8°15'E	30	GAW Antarctic coast	Feb 1983–Jan 2008

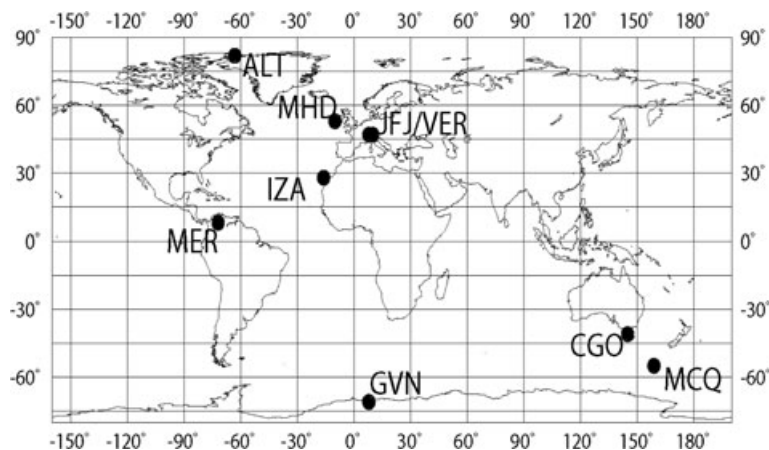


Fig. 1. Map of IUP-Heidelberg $^{14}\text{CO}_2$ sampling sites: ALT: Alert, CGO: Cape Grim, GVN: Neumayer, IZA: Izaña, JFJ: Jungfrauoch, MCQ: Macquarie Island, MHD: Mace Head, MER: Mérida Observatory, VER: Vermunt.

atmospheric mixing ratios of all three CO_2 isotopomers ($^{12}\text{CO}_2$, $^{13}\text{CO}_2$ and $^{14}\text{CO}_2$) from given boundary conditions; the actual time step varies with the model's dynamics; the maximum time step is ca. one week. GRACE is also capable of simulating atmospheric sulphur hexafluoride (SF_6), beryllium-7 and beryllium-10 mixing ratios, which serve mainly as tracers for atmospheric transport. The core of GRACE consists of an atmospheric module with 28 boxes, representing zonal mean tracer mixing ratios in six zonal and four (tropics) respectively five (extra-tropics) vertical subdivisions. Air mass (and tracer) exchange between the atmospheric boxes is controlled by three processes: (1) (turbulent) diffusive exchange between neighbouring boxes, (2) the Brewer–Dobson circulation and (3) lifting respectively lowering of the extra-tropical tropopause. Air mass exchange in GRACE is optimized using the observed atmospheric tracers $\Delta^{14}\text{CO}_2$ (only during the bomb and immediate post bomb era), SF_6 and the $^{10}\text{Be}/^7\text{Be}$ ratio as constraints.

In each zonal subdivision, the GRACE atmosphere is coupled to a terrestrial biosphere module comprising of three well-mixed carbon pools with different carbon mass and turnover times, representing living and dead biomass with different biochemical composition and degradation states. Net primary productivity as well as land-use change carbon fluxes and net biospheric uptake of anthropogenic CO_2 are prescribed for each pool. Atmosphere–ocean carbon and carbon isotope exchange are calculated during the initialization of the model from reconstructed time series of the atmospheric and sea surface CO_2 partial pressure, from reconstructed time series of the sea surface and atmospheric $\delta^{13}\text{C}$ and $\Delta^{14}\text{C}$ signatures and from assumptions about the gas exchange; it is thus pre-determined for each model run. This means that, in contrast to atmosphere–biosphere exchange, there is no feedback in the model between simulated atmospheric CO_2 mixing ratios (and its $\delta^{13}\text{C}$ and $\Delta^{14}\text{C}$ signatures) and the carbon isotope exchange between the ocean and the atmosphere. This means that changes in the oceanic boundary conditions (e.g. changes in the global mean piston velocity)

have a stronger impact on simulated atmospheric $\Delta^{14}\text{C}$ than they would have in the case of a fully coupled model. The carbon cycle in GRACE further comprises CO_2 fluxes ($^{12}\text{CO}_2 + ^{13}\text{CO}_2$) due to fossil fuel combustion and cement production. In addition to natural $^{14}\text{CO}_2$ production, anthropogenic $^{14}\text{CO}_2$ release from atmospheric nuclear bomb tests and nuclear industry are taken into account. Basic parameters of the global carbon cycle as implemented in GRACE are summarized in Table 2; a more comprehensive description of GRACE as well as its validation of transport can be found in the Supplementary Information. For this, we ran GRACE from pre-bomb times (1940) through the entire bomb-era through 2009.

2.3. Calculation of components of simulated atmospheric $\Delta^{14}\text{CO}_2$

In the following paragraph, we describe how we calculate the components of the spatial and temporal variability of $\Delta^{14}\text{C}$ from the GRACE results, in order to assign observed features to certain source/sink processes. GRACE simulates absolute concentrations of $^{12}\text{CO}_2$, $^{13}\text{CO}_2$, and $^{14}\text{CO}_2$, which for comparison with observations need to be transferred to $\Delta^{14}\text{CO}_2$ values. $\Delta^{14}\text{C}$ (in ‰) is defined according to Stuiver and Polach (1977) as

$$\Delta^{14}\text{C} = \left\{ \frac{A_S}{A_{ABS}} \left[1 - \frac{2 \cdot (25 + \delta^{13}\text{C}_S)}{1000} \right] - 1 \right\} \times 1000 \quad (1)$$

where A_S is the (measured) specific radiocarbon activity (in Bq/gC) of the sample, $A_{ABS} = 0.95 \cdot 0.238$ Bq/gC is the absolute specific activity of the radiocarbon standard (i.e. 95% of the activity of the OxA-I standard) and $\delta^{13}\text{C}_S$ is the $\delta^{13}\text{C}$ signature vs. VPDB of the sample.

Because GRACE does not simulate the specific radiocarbon activity A_S in a model box, this must be calculated from n^{14} and n^C , which are the number of ^{14}C , respectively total C atoms

Table 2. Parameters used in the model simulations of GRACE presented in Figs. 3, 5, 6, 7, 8, and 9

Flux components		Reference
Biospheric fluxes		
NPP total flux	47.5 PgC yr ⁻¹	Based on Naegler and Levin (2009b)
NPP meridional distribution		Cramer et al. (1999)
Net uptake anthropogenic CO ₂	54% of total (bio + oce) uptake (long-term average)	Consistent with Rayner et al. (1999), Prentice et al. (2001), Piper et al. (2001); Le Quéré et al. (2003) and Sabine et al. (2004)
Land-use change		Houghton (2003)
¹³ C fractionation	-18‰	C3 plants only, Degens (1969)
¹⁴ C Assimilation	Atmospheric ¹⁴ CO ₂	Levin et al. (1985), Manning et al. (1990), Manning and Melhuish (1994), Nydal and Lövseth (1996), Vogel et al. (2002), Levin and Kromer (2004), Levin et al. (2008)
¹⁴ C Respiration	Calculated with GRACE biosphere	Based on Naegler and Levin (2009b)
Oceanic fluxes		
<i>k</i> - <i>u</i> relationship	Quadratic	Wanninkhof (1992)
Zonal wind speed distribution	ECMWF	Gibson et al. (1997)
Global mean <i>k</i>	15.5 cm h ⁻¹	This study, adjusted to match ocean excess ¹⁴ C inventory constraints, consistent with Naegler (2009)
Oceanic excess ¹⁴ C inventory	253/383 × 10 ²⁶ atoms (1975/1995)	Naegler et al. (2006), Naegler (2009)
Net uptake anthropogenic CO ₂	46% of total (bio + oce) uptake (long-term average)	Consistent with Rayner et al. (1999), Prentice et al. (2001), Piper et al. (2001); Le Quéré et al. (2003) and Sabine et al. (2004)
¹³ C surface water		Quay et al. (2003)
¹³ C fractionation sea-air	-10.6‰	Morimoto et al. (2000) with SST from Levitus et al. (1998)
¹⁴ C surface water		Broecker et al. (1985) (pre-bomb and GEOSECS), Key et al. (2004) (WOCE), linearly extrapolated after 1995
Fossil fuel fluxes		
CO ₂ fluxes		Marland et al. (2007)
δ ¹³ C of fossil fuel CO ₂		Andres et al. (1996)
¹⁴C production		
Nuclear industry	Total: 12 × 10 ²⁶ atoms	UNSCEAR (2000), linearly extrapolated
Natural ¹⁴ C production	2.1 × 10 ²⁶ atoms yr ⁻¹	Lingenfelter (1963), based on Naegler and Levin (2006)
Bomb ¹⁴ C production	Total: 620 × 10 ²⁶ atoms	Naegler and Levin (2006, 2009a), based on nuclear explosions data base from Yang et al. (2000)

(¹²C + ¹³C + ¹⁴C) in the respective model box

$$A_S = \frac{\lambda \cdot N_A}{m_C} \cdot \frac{n^{14}}{n^C} \quad (2)$$

where $\lambda = 3.8332 \times 10^{-12} \text{ s}^{-1}$ is the decay constant of radio-carbon, $N_A = 6.022 \times 10^{23}$ the Avogadro Number and $m_C = 12.011 \text{ g}$ the molar mass of carbon. We then obtain from eq. (1)

$$\Delta^{14}\text{C} = \left\{ \frac{\lambda N_A}{A_{\text{ABS}} m_C} \frac{n^{14}}{n^C} \left[1 - \frac{2(25 + \delta^{13}\text{C})}{1000} \right] - 1 \right\} \times 1000. \quad (3)$$

In the case of a constant $\delta^{13}\text{C}$ value of -7‰ , we obtain

$$\Delta^{14}\text{C} = f \frac{n^{14}}{n^C} - 1000 \quad (4)$$

with the dimensionless factor $f = 8.19 \times 10^{14}$. Note that due to changes in atmospheric $\delta^{13}\text{C}$, f changes with time. However, in this study, this change is negligible compared to changes in n^{14} and n^C . Equation (4) now allows further investigating the components driving the observed spatial and temporal variability of atmospheric $\Delta^{14}\text{CO}_2$, as described in the following subsections.

2.3.1. Components of the simulated atmospheric $\Delta^{14}\text{CO}_2$ trend. According to eq. (4), the temporal change of $\Delta^{14}\text{C}$ can be calculated as

$$\frac{d}{dt} \Delta^{14}\text{C} = f \left[\frac{1}{n^C} \frac{dn^{14}}{dt} - \frac{n^{14}}{(n^C)^2} \frac{dn^C}{dt} \right]. \quad (5)$$

We investigate a number of processes P, which may change the total radiocarbon (and total carbon) content and thus the $\Delta^{14}\text{C}$ signature of an air mass. These processes include source/sink processes such as air–sea gas exchange, biospheric assimilation and respiration, fossil fuel-derived CO_2 emissions and (natural and anthropogenic) radiocarbon production. On the other hand, atmospheric transport processes (e.g. interhemispheric exchange or STE) may also change the atmospheric (radio-)carbon level. Due to the long mean lifetime of ^{14}C (8267 yr), radioactive decay is negligible in the context of this study.

If $(\frac{dn^{\text{C}}}{dt})_{\text{P}}$ and $(\frac{dn^{14}}{dt})_{\text{P}}$ denote the change of the carbon and radiocarbon content of an air mass (with composition n^{C} , n^{14}) due to process P, then the associated change in $\Delta^{14}\text{C}$ (denoted $\frac{d}{dt}\Delta^{14}\text{C}_{\text{P}}$) can be split into different components

$$\frac{d}{dt}\Delta^{14}\text{C}_{\text{P}} = f \left[\frac{1}{n^{\text{C}}} \frac{dn^{14}}{dt} - \frac{n^{14}}{(n^{\text{C}})^2} \frac{dn^{\text{C}}}{dt} \right]_{\text{P}}. \quad (6)$$

Equation (6) allows calculating the contribution of each process P to the temporal change of, for example, simulated hemispheric tropospheric mean $\Delta^{14}\text{CO}_2$ if the individual changes in the radiocarbon and carbon inventory due to process P are known. The results of this component analysis are presented and discussed in Section 4.2.

2.3.2. Components of the simulated interhemispheric $\Delta^{14}\text{CO}_2$ difference. In order to investigate the components of the interhemispheric $\Delta^{14}\text{CO}_2$ difference – for simplicity – we applied here a simple 2-box model approach: the tracer concentration difference δC (in mol per mass air) between the northern (NH) and the southern hemisphere (SH) can be calculated (for constant sources and sinks) as

$$\delta C = C_{\text{NH}} - C_{\text{SH}} = \frac{\tau}{2m} (F_{\text{NH}} - F_{\text{SH}}) \quad (7)$$

(Jacob et al., 1987; Levin and Hesshaimer, 1996). Here m denotes the air mass of each hemisphere, τ is the turnover time for air mass exchange between both hemispheres and F denotes the net flux of the tracer into or out of each hemisphere (in mol per year), but *excluding* the tracer exchange flux *between* the two hemispheres. It further holds for each hemisphere, that concentration changes are caused by (net) tracer fluxes into each hemisphere, that is,

$$\frac{d}{dt}C = \frac{F}{m} \Leftrightarrow F = m \frac{d}{dt}C. \quad (8)$$

With eqs (5) and (8), we may now define a Δ -flux F_{Δ} as follows

$$F_{\Delta} = m \frac{d}{dt}\Delta^{14}\text{C} \quad (9)$$

$$= mf \left[\frac{1}{n^{\text{C}}} \frac{dn^{14}}{dt} - \frac{n^{14}}{(n^{\text{C}})^2} \frac{dn^{\text{C}}}{dt} \right]. \quad (10)$$

The Δ -flux F_{Δ} (eqs 9 and 10) acts in a similar manner as the mass flux F (eq. 8): while in case of a mass flux the mixing ratio of the tracer in question is changed, a Δ -flux F_{Δ} changes

the Δ -signature of the considered air mass. Thus, differences in F_{Δ} between two neighbouring boxes result in spatial $\Delta^{14}\text{C}$ differences between these boxes, in a similar manner as different mass fluxes F cause spatial CO_2 mixing ratio gradients. We therefore obtain analogous to eq. (7) for the interhemispheric $\Delta^{14}\text{C}$ difference ($\delta\Delta^{14}\text{C}$)

$$\delta\Delta^{14}\text{C} = \Delta^{14}\text{C}_{\text{NH}} - \Delta^{14}\text{C}_{\text{SH}} \quad (11)$$

$$= \frac{\tau}{2m} (F_{\Delta}^{\text{NH}} - F_{\Delta}^{\text{SH}}) \quad (12)$$

$$= \frac{\tau f}{2} \sum_{\text{P}} \left[\frac{1}{n^{\text{C}}} \frac{dn^{14}}{dt} - \frac{n^{14}}{(n^{\text{C}})^2} \frac{dn^{\text{C}}}{dt} \right]_{\text{P}}^{\text{NH}} - \left[\frac{1}{n^{\text{C}}} \frac{dn^{14}}{dt} - \frac{n^{14}}{(n^{\text{C}})^2} \frac{dn^{\text{C}}}{dt} \right]_{\text{P}}^{\text{SH}} \quad (13)$$

$$= \sum_{\text{P}} \delta\Delta^{14}\text{C}_{\text{P}}. \quad (14)$$

Equation (13) allows calculating the effect of each process P contributing to the interhemispheric $\Delta^{14}\text{C}$ difference if the temporal changes in the hemispheric radiocarbon and total carbon inventory due to process P are known. As mentioned before, in this approach, the interhemispheric exchange must not be included as a process. The scheme developed here for two hemispheric boxes can easily be generalized for any two neighbouring compartments of the atmosphere (e.g. for STE).

Note, however, that this approach is only exactly valid in the case of a two-box system and temporally constant sources and sinks. But as long as the characteristic time scale of changes of the fluxes involved is large compared to the interhemispheric exchange time ($\tau \approx 1$ year), eq. (7) is a good approximation. In our GRACE simulations, the sum of the components of the north–south $\Delta^{14}\text{C}$ difference are thus approximately identical with the simulated tropospheric mean north–south $\Delta^{14}\text{C}$ difference, except for times of strong changes of the fluxes F_{Δ} (and corresponding strong changes in the N–S difference).

2.3.3. Components of the simulated $\Delta^{14}\text{CO}_2$ seasonal cycle. All seasonally varying source and sink processes as well as seasonally varying atmospheric mixing – both horizontally and vertically – contribute to the seasonal cycle of $\Delta^{14}\text{C}$ in atmospheric CO_2 . However, atmospheric mixing between two compartments contributes to the $\Delta^{14}\text{C}$ seasonality *only if* there are $\Delta^{14}\text{C}$ differences between these compartments. There are thus two fundamentally different approaches to define the components of the $\Delta^{14}\text{C}$ seasonal cycle, which either explicitly include the effect of atmospheric mixing on the $\Delta^{14}\text{C}$ seasonality (Definition 1) or attribute the $\Delta^{14}\text{C}$ seasonal cycle exclusively to the fundamental source and sink processes (such as natural and anthropogenic ^{14}C production, atmospheric $^{14}\text{CO}_2$ exchange with ocean and biosphere, and fossil fuel-derived CO_2 emissions, Definition 2).

Here in this study, we calculate components of $\Delta^{14}\text{CO}_2$ seasonal cycles according to both definitions. A comparison of results from Definitions 1 and 2 allows for a quantitative understanding of how both, atmospheric mixing and source and sink processes, contribute to the $\Delta^{14}\text{C}$ seasonality (compare Section 4.4).

Definition 1. The contribution of each process P (comprising source and sink processes S and mixing processes T) to the simulated $\Delta^{14}\text{C}$ seasonality can be calculated as the difference between the $\Delta^{14}\text{C}$ seasonal cycle from a full model run (denoted $\Delta^{14}\text{C}_{\text{full}}$) and the seasonal cycle from a model run where *only the seasonality of the process* in question is *turned off* ($\Delta^{14}\text{C}_{\text{NoSP}}$; index NoSP: ‘No seasonality process P’)

$$\Delta^{14}\text{C}_P^{\text{seas},1} = \Delta^{14}\text{C}_{\text{full}} - (\Delta^{14}\text{C})_{\text{NoSP}}, \quad (15)$$

where $\Delta^{14}\text{C}_P^{\text{seas},1}$ denotes the contribution of process P to the $\Delta^{14}\text{C}$ seasonal cycle according to Definition 1. In this definition, seasonally varying atmospheric mixing such as tropospheric cross-equator exchange (CEE) and STE contributes to the $\Delta^{14}\text{C}$ seasonality in a similar manner as seasonally varying sources and sinks.

Definition 2. Alternatively, we may wish to focus our analysis of the components of the tropospheric $\Delta^{14}\text{C}$ seasonality on the fundamental sources and sinks of $\Delta^{14}\text{C}$. As mentioned above, seasonally varying large scale atmospheric transport (STE or CEE) contributes to the seasonality of $\Delta^{14}\text{C}$ *only* because source/sink processes have caused vertical (relevant for STE) or horizontal (relevant for CEE) $\Delta^{14}\text{C}$ differences. For example, fossil fuel-derived CO_2 emissions occur mainly in the northern troposphere. They deplete $\Delta^{14}\text{C}$ in northern tropospheric CO_2 with respect to both the southern troposphere and the northern stratosphere. Seasonally varying STE (or CEE) mixes $\Delta^{14}\text{C}$ depleted air masses with $\Delta^{14}\text{C}$ enriched air masses, resulting in a seasonal cycle of atmospheric $\Delta^{14}\text{C}$. The larger the horizontal (or vertical) $\Delta^{14}\text{C}$ difference caused by source/sink process S, the larger the contribution of process S to the component of the $\Delta^{14}\text{C}$ seasonal cycle caused by seasonally varying CEE (or STE). Thus, if the contribution of each source/sink process S to the large-scale horizontal or vertical gradient is known, the components of the $\Delta^{14}\text{C}$ seasonal cycle due to seasonally varying large-scale atmospheric mixing as calculated according to Definition 1 may be further split into contributions from each $\Delta^{14}\text{C}$ source/sink process S (e.g. fossil CO_2 emissions, exchange with biosphere or ocean, natural or anthropogenic ^{14}C production). For each source/sink process S, we thus obtain a contribution to the $\Delta^{14}\text{CO}_2$ seasonality due to seasonally varying source/sink strength (from Definition 1) and due to seasonally varying atmospheric transport. For each source/sink process S, the sum of

these two contributions is the component of process S according to Definition 2.

Formally, we proceed as follows: eq. (11) shows that the total $\Delta^{14}\text{CO}_2$ *difference* between two atmospheric compartments ($\delta\Delta^{14}\text{C}$) can be split into the contribution of each source/sink process S ($\delta\Delta^{14}\text{C}_S$). We can thus calculate the relative contribution of each source/sink process S to the $\Delta^{14}\text{CO}_2$ *difference* $\delta\Delta^{14}\text{C}$ as

$$a_S = \frac{\delta\Delta^{14}\text{C}_S}{\delta\Delta^{14}\text{C}}. \quad (16)$$

Note that from the definition of $\delta\Delta^{14}\text{C}_S$ (see eq. 14) it holds that $\sum a_S = 1$, with a_S potentially ranging from $-\infty$ to $+\infty$. Furthermore, from Definition 1 (eq. 15), we know the contribution of the transport process T (i.e. CEE or STE) to the $\Delta^{14}\text{C}$ seasonal cycle, which is denoted $\Delta^{14}\text{C}_T^{\text{seas},1}$ here. We can thus calculate the contribution of the source/sink process S to $\Delta^{14}\text{C}_T^{\text{seas},1}$ as

$$\Delta^{14}\text{C}_{S(T)}^{\text{seas}} \equiv a_S \Delta^{14}\text{C}_T^{\text{seas},1}. \quad (17)$$

The total contribution of source/sink process S to the seasonal variation of $\Delta^{14}\text{C}$ ($\Delta^{14}\text{C}_S^{\text{seas},2}$, Definition 2) is the sum of the contribution of the seasonal variability of the source/sink S ($\Delta^{14}\text{C}_S^{\text{seas},1}$, Definition 1, see eq. 15) and the contribution of S via seasonally varying atmospheric transport ($\Delta^{14}\text{C}_{S(T)}^{\text{seas}}$, eq. 17):

$$\Delta^{14}\text{C}_S^{\text{seas},2} = \Delta^{14}\text{C}_{S(T)}^{\text{seas}} + \Delta^{14}\text{C}_S^{\text{seas},1}. \quad (18)$$

2.3.4. Components of the simulated interannual variability in $\Delta^{14}\text{CO}_2$. In the standard simulation of GRACE, we assume no interannual variability in the air–sea gas exchange, in atmospheric mixing (STE and CEE), in biospheric photosynthesis (NPP) or heterotrophic respiration (RES). Furthermore, natural radiocarbon production is assumed to follow an exact sinusoidal 11-yr solar cycle, neglecting a stronger year-to-year variability in the sun’s activity. Finally, interannual variability of land-use change CO_2 fluxes is given by Houghton (2003), which might be too low. We have estimated the contribution of interannual variability of these processes to interannual variability in atmospheric $\Delta^{14}\text{C}$ by comparing the standard model run with a model run where interannual variability of these processes (respectively stronger variability for natural ^{14}C production and land-use change CO_2 fluxes) of reasonable amplitude is taken into account (index NoIVP: ‘no Interannual Variability of process P’, index IVP: ‘Interannual Variability for process P on’).

$$\Delta^{14}\text{C}_P^{\text{IV}} = \Delta^{14}\text{C}_{\text{NoIVP}} - \Delta^{14}\text{C}_{\text{IVP}}. \quad (19)$$

2.4. Calculation of de-trended average seasonal cycles

To calculate the de-trended average seasonal cycles for the observations as well as the model output, we first calculated a

polynomial fit (Nakazawa et al., 1997) through the individual data points. The residuals from the fit curve were linearly interpolated to a daily time axis, before we calculated monthly means for the entire period of data availability. Finally, we calculated mean values, SD σ and the error of the mean value ($= \sigma/\sqrt{n}$, where n denotes the number of data averaged for January, February, etc. in the period of focus).

3. Observations

CO_2 and carbon isotopic observations from globally distributed background stations are available since the 1950s. In addition there are measurements published on air included in ice cores as well as ^{14}C measurements from tree rings. We use these published data for model validation in the Supplementary Information and also in Section 4.1 where we show GRACE simulations for the whole period of investigation (1940 until the present). Reference to these earlier data is given in the respective sections. Except for Section 3.1, we present here only our new data set from the Heidelberg global observational network of background measurements which has not been published before. These as earlier Heidelberg data are available via web access (http://www.iup.uni-heidelberg.de/institut/forschung/groups/kk/Data_html) or on request to I.L.

3.1. Observed global atmospheric $\Delta^{14}\text{CO}_2$ distribution and trends from pre-bomb times until the present

The most prominent atmospheric $^{14}\text{CO}_2$ perturbation took place in the 1950s and 1960s when large amounts of artificial ^{14}C were produced during atmospheric nuclear weapon tests. This artificial production led to an increase of the $^{14}\text{C}/\text{C}$ ratio in atmospheric CO_2 of the northern hemisphere by a factor of two in 1962/1963. The southern hemispheric $\Delta^{14}\text{CO}_2$ increase was delayed by about 1–2 years (Fig. 2), reflecting the hemispheric mixing time of air masses in the troposphere (Czeplak and Junge, 1974). After the nuclear test ban treaty in 1963 the atmospheric $^{14}\text{CO}_2$ spike decreased almost exponentially due to penetration of bomb $^{14}\text{CO}_2$ into the other carbon reservoirs (ocean and biosphere). The seasonal $\Delta^{14}\text{CO}_2$ variations in the 1960s at northern hemispheric stations as shown here for Vermont (but which are also observed at other sites like Fruholmen, Lindesnes and Spitsbergen, Nydal and Lövseth, 1996) mainly stem from seasonally varying STE: Most of the bomb ^{14}C was injected into the stratosphere from where it was transported only with some delay into the troposphere. This prominent signal was used in the present study to constrain stratosphere–troposphere air mass exchange in the GRACE model as well as air mass transport within the stratosphere itself (compare Fig. S6). The bomb-induced spatial $\Delta^{14}\text{CO}_2$ gradients in the atmosphere homogenized in the 1970s, making the tropospheric $\Delta^{14}\text{CO}_2$ distribution and its temporal variations now mainly governed by fossil fuel CO_2 emissions as well as by surface exchange processes (including

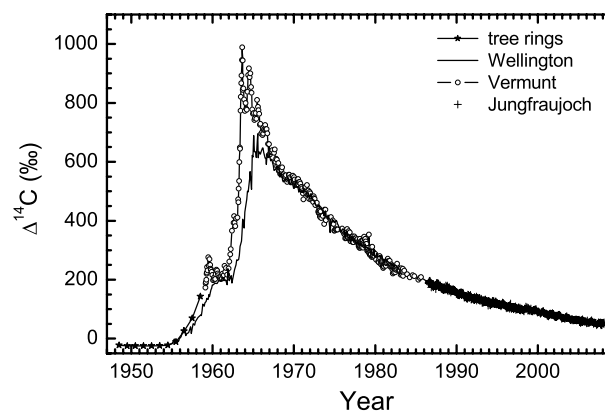


Fig. 2. Temporal change of observed atmospheric $\Delta^{14}\text{CO}_2$ in the northern and the southern hemisphere. The (northern hemispheric) tree-ring data were taken from Stuiver and Quay (1981) and Hua and Barbetti (2004). The early Wellington data (Southern Hemisphere) was taken from Manning et al. (1990).

isotope disequilibrium fluxes with the ocean and the biosphere). These features will be quantitatively discussed together with the GRACE simulation results in Section 4.2.

3.2. Observed meridional distribution of $\Delta^{14}\text{CO}_2$ in the last two decades

The meridional gradient of tropospheric $\Delta^{14}\text{CO}_2$ has become very small in the last two decades (of order of a few permil only). Figure 3b shows the mean meridional distribution of $\Delta^{14}\text{CO}_2$ for 1994–1997, when global coverage of our Heidelberg data is best (Table 1). The corresponding mean meridional profile of CO_2 mixing ratios in the marine boundary layer (GLOBALVIEW- CO_2 , 2008) is shown in Fig. 3a for comparison. If the north–south difference of about 3–4 ppm CO_2 at that time were due to a pure fossil fuel CO_2 signal, we would then expect about a 10‰ higher $\Delta^{14}\text{C}$ in the south compared to the north. This is obviously not the case and points to an additional net $\Delta^{14}\text{CO}_2$ source in the north or an equivalent net $\Delta^{14}\text{CO}_2$ sink in the southern atmosphere. One candidate that depletes $\Delta^{14}\text{CO}_2$ at mid-to-high southern latitudes is the strong ^{14}C disequilibrium flux between the atmosphere and ^{14}C -depleted surface ocean water around Antarctica (compare Fig. 3c). This disequilibrium flux is most prominent between 50°S and 70°S where wind speed makes gas exchange fluxes largest (Kalney et al., 1996; Gibson et al., 1997) (see the most strongly influenced atmospheric $\Delta^{14}\text{CO}_2$ at Macquarie Island, 55°S in Fig. 3b). The observed $\Delta^{14}\text{CO}_2$ increase towards the South Pole (open star in Fig. 3b, which was extrapolated from South Pole data of the years 1987 and 1989 published by Meijer et al. (2006), assuming a constant difference between Neumayer and South Pole) corroborates the assumption that our sites at Neumayer and Macquarie Island are

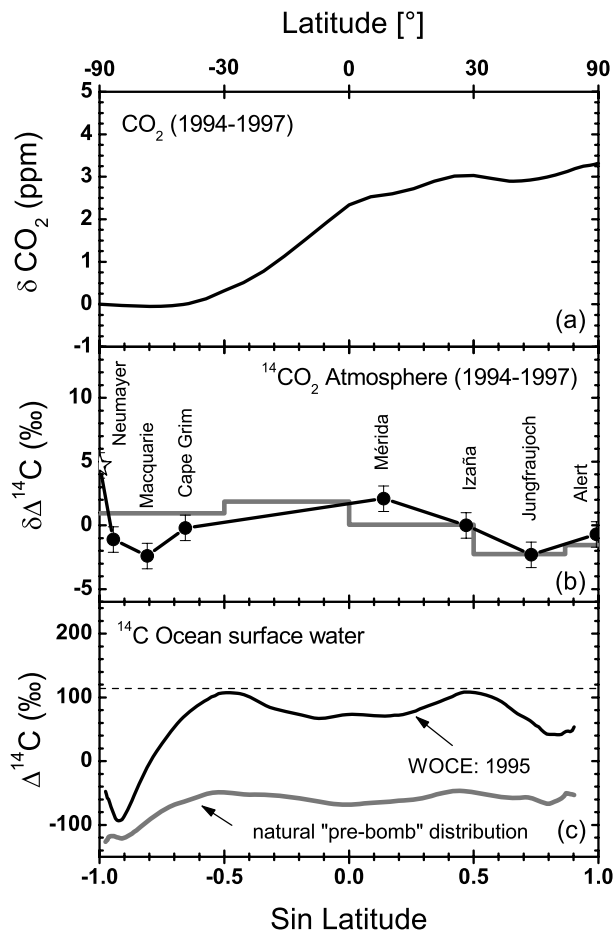


Fig. 3. Mean meridional profiles 1994–1997 of (a) CO_2 mixing ratio (data from GLOBALVIEW-CO2 (2008)) relative to South Pole and (b) $\delta^{14}\text{C}$ in atmospheric CO_2 at stations from the Heidelberg network (see Table 1) supplemented by observations from South Pole (open star) by Meijer et al. (2006) extrapolated from measurements in 1987 and 1989, assuming a constant difference between Neumayer and South Pole. Mean values simulated by GRACE for the six tropospheric boundary layer boxes are included as grey lines (histogram). $\delta\Delta^{14}\text{C}$ is plotted relative to the mean observed value of all stations shown, respectively the simulated global mean $\Delta^{14}\text{C}$. (c) Zonal mean $\Delta^{14}\text{C}$ of dissolved inorganic carbon (DIC) in surface ocean water for the mid-1990s derived from cruises of the WOCE experiment and estimates of the pre-bomb zonal mean sea surface $\Delta^{14}\text{C}$ (Key et al. 2004). The 1994–1997 mean tropospheric $\Delta^{14}\text{CO}_2$ value is indicated as dashed line.

strongly influenced by ocean $\Delta^{14}\text{CO}_2$ fluxes, whereas South Pole is rather influenced by stratospheric air masses with high $\Delta^{14}\text{C}$. The $\Delta^{14}\text{CO}_2$ dip in mid latitudes of the northern hemisphere, visible at Jungfraujoch, is an effect of northern hemispheric and possibly also regional European ^{14}C -free fossil fuel CO_2 emissions.

All individual measurements from our globally distributed stations are displayed in Figs. 4a–e together with deseasonalized trend curves calculated for the individual data

sets using the fit routine from Nakazawa et al. (1997) and a cut-off frequency of 52 months. The smoothed long-term $\Delta^{14}\text{CO}_2$ differences between the trend curves of individual sites (Figs. 4a–d) and the trend curve calculated through the Neumayer data (Fig. 4e) are displayed in Fig. 4f: The $\Delta^{14}\text{CO}_2$ differences relative to Neumayer at the northern hemispheric sites show a steady decrease from values between $\delta\Delta^{14}\text{C} = +4\text{‰}$ to $+6\text{‰}$ in the late 1980s to -2‰ to -6‰ in the last five years, with very similar mean values and trends seen at stations north of 45°N , that is, Jungfraujoch, Mace Head and Alert. For the overlapping periods, mean differences between Alert and Jungfraujoch were at $0.6 \pm 0.5\text{‰}$ (1987–2007), whereas the Mace Head and Jungfraujoch difference (2001–2007) is $1.0 \pm 0.5\text{‰}$. The $\Delta^{14}\text{CO}_2$ depletion observed at Jungfraujoch compared to Mace Head and Alert is likely caused by a small surplus of continental fossil fuel CO_2 seen at Jungfraujoch (compared to pristine northern hemispheric clean marine air). $\Delta^{14}\text{CO}_2$ at Izaña (28°N) and Mérida Observatory (8°N) show the highest values throughout its observational period. Mean differences of Izaña $\Delta^{14}\text{CO}_2$ compared to the Neumayer fit curve (1984–2001) (Fig. 4f) are $3.7 \pm 0.6\text{‰}$ while the respective difference for Mérida Observatory (1991–1997) is $3.6 \pm 0.4\text{‰}$.

In the second half of the 1980s, we observe interesting $\Delta^{14}\text{CO}_2$ excursions from the Neumayer fit curve: $\Delta^{14}\text{CO}_2$ data at Cape Grim (41°S) are up to 6‰ higher than at Neumayer (71°S), while for the rest of the time differences between the two sites are only between 1 and 3‰ . During the second half of the 1980s the stations in the northern hemisphere (Alert, Jungfraujoch and in particular Izaña) also show a very large difference to the Neumayer long-term trend. This $\Delta^{14}\text{C}$ excursion roughly coincides with an El Niño Southern Oscillation (ENSO) event and may indicate the release of ^{14}C -rich CO_2 from the (tropical) biosphere. However, no such ‘bump’ is observed during the strong El Niño in 1997–1998 (Multivariate ENSO Index (MEI) available from <http://www.cdc.noaa.gov/people/klaus.wolter/MEI/>). As will be discussed in detail in Section 4.5, GRACE fails in simulating the amplitude of the interannual variability in both the $\Delta^{14}\text{C}$ growth rate and the interhemispheric $\Delta^{14}\text{C}$ difference, pointing to serious gaps in our understanding of the mechanisms controlling the interannual $\Delta^{14}\text{C}$ variability.

3.3. Observed seasonal cycles of $\Delta^{14}\text{CO}_2$

For comparison of the seasonal cycles among the globally distributed sites, we selected the period from 1995–2005, where observations from all sites are available, at least for certain periods (Table 1). Seasonal cycle peak-to-trough amplitudes are between 5‰ (Jungfraujoch) and 7‰ (Alert) at mid to high northern latitudes, whereas at Izaña the seasonal cycle is only half as pronounced, showing an amplitude of about 3‰ with a dip in September (Fig. 5). In the southern hemisphere, a seasonal cycle of only ca. 2‰ is observed at Cape Grim. No significant seasonality is observed at Neumayer, Macquarie Island or Mérida.

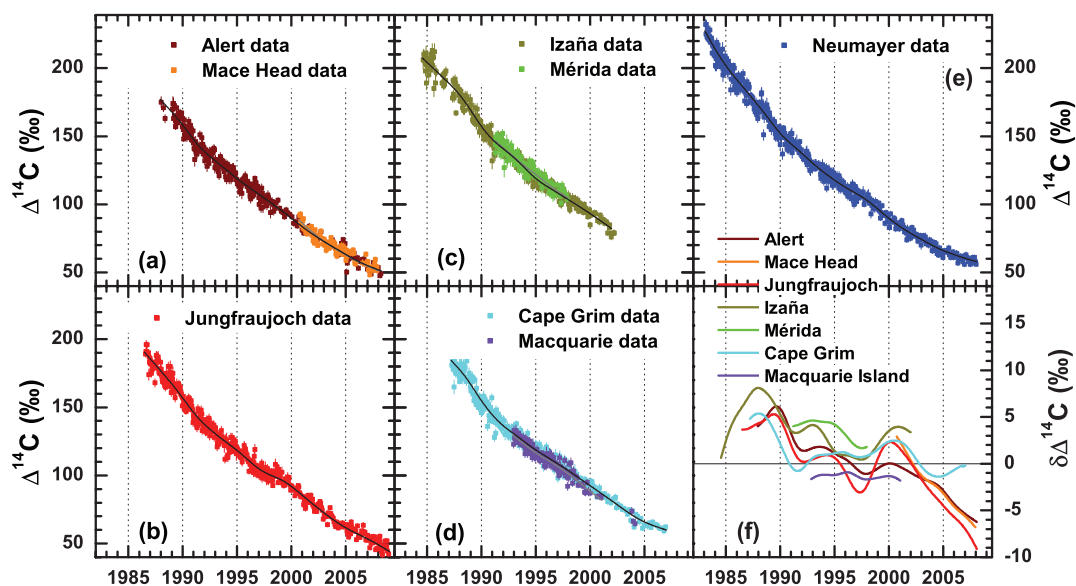
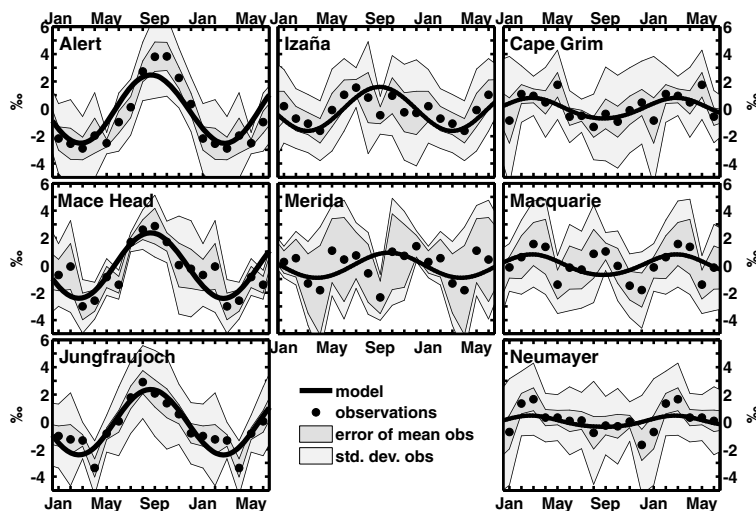


Fig. 4. (a–e) Measured $\Delta^{14}\text{CO}_2$ at the Heidelberg background stations (error bars are 1σ); the smooth curves are de-seasonalised trend curves fitted through the data using the fit routine from Nakazawa et al. (1997) with a cut-off frequency of 52 months (plotted as grey curves for the shorter records). (f) Observed long-term trends of $\Delta^{14}\text{CO}_2$ differences between the Neumayer fit curve and those of the other observational sites in the northern and in the southern hemisphere.

Fig. 5. Observed and GRACE simulated mean seasonal cycles (1995–2005) of atmospheric $\Delta^{14}\text{CO}_2$ at Alert respectively the northern polar latitudes (NHP), Mace Head (NHM), Jungfraujoch (NHM), Izaña (mean of NHT and NHM), Mérida (NHT), Cape Grim (SHM), Macquarie Island (NHM) and Neumayer (Antarctica) (SHP). Left-hand column: northern extra-tropics, middle column: tropics, right-hand column: southern extra-tropics. Note that after December, we repeated the first six months of the mean seasonal cycle to better show the full amplitude. Light grey bands give the 1σ SD of the de-trended observed monthly means, while smaller dark grey bands give the error of the mean values (see Section 2.4. for details).



Our data would allow inferring temporal changes of the seasonal cycles at Alert, Jungfraujoch and Cape Grim. However, only at Alert and Jungfraujoch do we see a slight decrease of the amplitude by ca. 1‰ between the 1990s and the 2000s. The phasing of the seasonal cycles in the Northern Hemisphere are very similar, in particular at Jungfraujoch and Mace Head with a maximum occurring around day 260 (mid-September) and minimum around day 90 (late March–early April). At Alert, the phasing is slightly shifted to later dates by about one month (compare Fig. 5).

4. Discussion of model simulations and comparison with observations

In the following section, the observational features of the global atmospheric CO_2 and carbon isotopic variability are compared with GRACE simulations. First, we investigate the overall trends of all isotopomers for the whole period of observations in both hemispheres. In subsequent sections we then concentrate only on $^{14}\text{CO}_2$ and its components contributing to the trends, gradients and seasonal variation, in particular, in comparison to our new

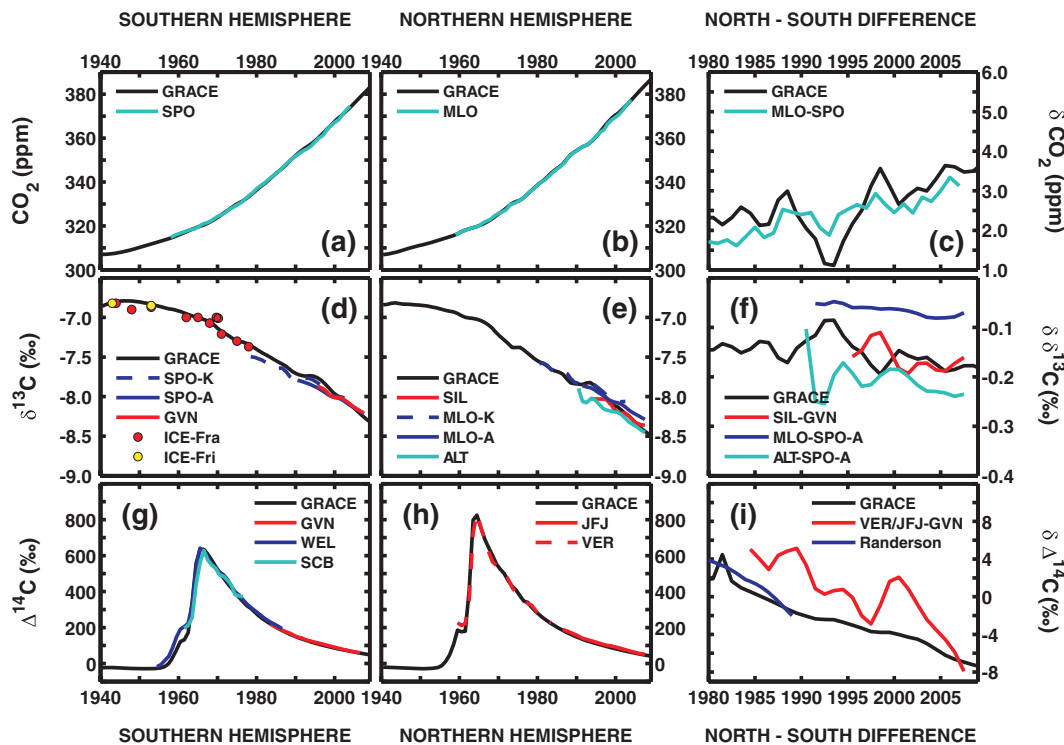


Fig. 6. Comparison of simulated (black lines in all panels) and observed annual mean atmospheric CO_2 mixing ratio (top row), $\delta^{13}\text{C}$ (middle row) and $\Delta^{14}\text{C}$ (bottom row). Left-hand column: southern hemisphere (model results from southern polar latitude box, SHP, $60^\circ\text{S} - 90^\circ\text{S}$); middle column: northern hemisphere (model results from northern mid-latitude box, NHM, $30^\circ\text{N} - 60^\circ\text{N}$), right-hand column: north-minus-south difference of each isotopomer. Note the different time axis of the right column. Observations are from the following stations: SPO: South Pole; MLO: Mauna Loa; GVN: Neumayer Station; ICE: Antarctic ice core data; SIL: Schauinsland; ALT: Alert; WEL: Wellington, SCB: Scott Base; JFJ: Jungfrauoch; VER: Vermunt. Randerson: Model results from Randerson et al. (2002). For references see main text. Uncertainties for the observed N-S differences: $\text{CO}_2 < 0.1\text{ppm}$, $\delta^{13}\text{C} < 0.02\text{‰}$, $\Delta^{14}\text{C} < 2\text{‰}$.

high precision global data set of the last two decades presented in Section 3.

4.1. GRACE model simulation of the global atmospheric CO_2 , $\delta^{13}\text{C}$ and $\Delta^{14}\text{C}$ trends

The challenge of the GRACE model simulations was to consistently reproduce not only atmospheric $\Delta^{14}\text{C}$ variations, but also CO_2 mixing ratios and $\delta^{13}\text{C}$ in both hemispheres from pre-bomb times (1940) until the present. This is crucial if we want to use the GRACE simulations to identify and quantify the processes contributing to the observed $\Delta^{14}\text{C}$ trends, gradients and seasonal cycles. Figure 6 compares the observed and simulated CO_2 mixing ratios and the $\delta^{13}\text{C}$ and $\Delta^{14}\text{C}$ signatures in atmospheric CO_2 for the northern and the southern hemispheres, as well as the north-minus-south difference of these quantities. As outlined in the Supplementary Information, the uptake of anthropogenic CO_2 by the biosphere in the model is adjusted in a way that the simulated global atmospheric carbon burden matches the observations. Thus, it is not a surprise that the simulated CO_2 mixing ratio trends match well with the observations

in the northern and southern hemispheres (Figs. 6a and b, observed CO_2 mixing ratios from Keeling et al., 2008). Also, the observed north–south CO_2 difference is generally matched well by GRACE (Fig. 6c). Note that we compare here the GRACE model simulations for the NHM and SHP boxes with the observations at mid latitudes of the northern hemisphere and mid and/or high latitudes in the southern hemisphere. Since the mixing between mid latitude and polar boxes in GRACE is rather fast, we simulate only small differences between these boxes (in particular in the southern hemisphere) in absence of strong $\Delta^{14}\text{C}$ sources and sinks (compare Fig. 3b).

The interannual variability of the north–south CO_2 difference is somewhat larger in GRACE than that observed. This is mainly due to the fact that strong interannual changes of the airborne fraction of anthropogenic CO_2 result in a strong variability of the biospheric uptake of anthropogenic CO_2 in GRACE. Since this uptake is assumed in the model to occur only in northern mid-latitudes (see Supplementary Information), variability of the airborne fraction translates into variability of the north–south difference of the CO_2 mixing ratio in our model.

Similar to CO_2 , GRACE reproduces the observed decrease in atmospheric $\delta^{13}\text{CO}_2$ in the last decades in both hemispheres well, as shown in Figs. 6d and e (data references: Keeling et al., 2005 (SPO-K, MLO-K); Allison et al., 2009 (SPO-A, MLO-A, ALT); Friedli et al., 1986 (ICE-Fri), Francey et al., 1999 (ICE-Fra) and unpublished Heidelberg data obtained from regular flask samples collected at Neumayer (GVN) and Schauinsland (SIL)). The interhemispheric $\delta^{13}\text{CO}_2$ difference as estimated by GRACE between northern mid latitudes (NHM: 30°N – 60°N) and southern polar latitudes (SHP: 60°S – 90°S) compares well with the observed $\delta^{13}\text{CO}_2$ difference between Schauinsland (SIL) and Neumayer (GVN) observations (red line in Fig. 6f). The observed $\delta^{13}\text{CO}_2$ difference between Alert (82°N) (respectively Mauna Loa, 19°N) and South Pole, based on data from Allison et al. (2009), is smaller (respectively larger) than the simulated $\delta^{13}\text{CO}_2$ difference between NHM and SHP in GRACE. This is probably due to the fact that neither Mauna Loa (19°N) nor Alert (82°N) are representative for the NHM box (30°N – 60°N) in GRACE. However, if we interpolate $\delta^{13}\text{CO}_2$ for a virtual northern mid-latitudes station from the Allison et al. (2009) data, the respective difference to South Pole agrees well with the simulated NHM-SHP $\delta^{13}\text{CO}_2$ difference (not shown).

As already shown by Naegler and Levin (2006), the simulated atmospheric long-term $\Delta^{14}\text{CO}_2$ trend in GRACE (Figs. 6g and h) agrees very well with the observations (WEL, SCB: Manning et al. (1990), GVN, JFJ, VER: this study) throughout most of the bomb era. Only just prior to the maximum tropospheric $\Delta^{14}\text{CO}_2$ reached in 1963, do the $\Delta^{14}\text{CO}_2$ simulation results slightly underestimate the observed $\Delta^{14}\text{CO}_2$, as is particularly evident in the southern hemisphere. GRACE tends to underestimate the observed north–south $\Delta^{14}\text{CO}_2$ difference by a few permil throughout the last decades (see also Fig. 3b). Furthermore, interannual variability in the observed north–south $\Delta^{14}\text{C}$ difference is not captured well in GRACE; however, the general decreasing trend of the north–south difference is reproduced. Also the amplitude and phase of the mean observed $\Delta^{14}\text{CO}_2$ seasonal cycles at both mid northern and at mid-southern (if significant) hemispheric sites are reproduced correctly by the model (see Fig. 5).

All together, we can conclude that – based on the most recent knowledge of atmospheric carbon fluxes published in the literature (see Table 2) – we are able to consistently simulate with GRACE the temporal development of global mean CO_2 , $\delta^{13}\text{CO}_2$ and $\Delta^{14}\text{CO}_2$ for the last 70 yr. We are also able to simulate the mid-latitude north–south differences of CO_2 and $\delta^{13}\text{CO}_2$ fairly well in the last 25 yr, where respective direct observations exist. However, we slightly underestimate the north–south difference in atmospheric $\Delta^{14}\text{CO}_2$ in the last 25 yr, on average, by ca. 3‰. In the following sections, it is thus justifiable to use the GRACE simulations to investigate the major processes contributing to the observed trends, seasonal cycles and also the north–south difference, but keeping in mind that the latter is not perfectly described by GRACE model simulations.

4.2. Simulated components of the global long-term $\Delta^{14}\text{CO}_2$ trend

Figure 7a shows the components of the long-term trend in tropospheric $\Delta^{14}\text{CO}_2$ between 1945 and 1980. During this period, the trend of $\Delta^{14}\text{CO}_2$ was clearly dominated by the input of radiocarbon from the stratosphere into the troposphere. This stratospheric component of the $\Delta^{14}\text{CO}_2$ trend, in turn, is controlled by the source of ‘bomb’ radiocarbon (mainly) in the stratosphere. This can be seen by comparing the magnitude of the stratospheric component of the trend after the onset of strong atmospheric bomb tests in 1954 with pre-bomb times (made up by only natural radiocarbon also largely entering the troposphere from the stratosphere). The strong, positive stratospheric forcing of the $\Delta^{14}\text{CO}_2$ trend was counteracted mainly by uptake of excess ^{14}C by the ocean (dark blue line in Fig. 7a) and the biosphere (green line). The resulting total trend remains negative after 1965, when oceanic and biospheric excess $^{14}\text{CO}_2$ uptakes exceed the stratospheric input of excess $^{14}\text{CO}_2$ into the troposphere.

This picture changes in the post-bomb period (i.e. after the last atmospheric nuclear bomb test in 1980): Atmospheric $\Delta^{14}\text{CO}_2$ continues to decrease (dashed black line in Figs. 7a and b), although with a decreasing rate, and after 1988 the dominant trend factor becomes the input of ^{14}C -free fossil fuel-derived CO_2 into the troposphere. A constant fossil trend component of ca. -12 to -14 ‰ per year is derived from the model, which at a first glance is surprising in view of the strongly increasing fossil CO_2 emissions (see discussion in Section 4.8). In the post-bomb period, the ocean uptake of (excess) ^{14}C still causes atmospheric $\Delta^{14}\text{CO}_2$ to decrease, however, the oceanic uptake component of the $\Delta^{14}\text{CO}_2$ trend has decreased from more than -20 ‰ per year in 1980 to less than -5 ‰ per year today. Throughout the last decades, the terrestrial biosphere has been a source of (excess) $^{14}\text{CO}_2$ to the atmosphere (Naegler and Levin, 2009a), resulting in a positive biospheric component in the $\Delta^{14}\text{CO}_2$ trend. Stratospheric input of (mostly natural) radiocarbon adds another $+5$ ‰ per year to the $\Delta^{14}\text{CO}_2$ trend (solid red line in Fig. 7b). The fact that the stratospheric component is rather constant after 1988 and of similar magnitude (but opposite in sign) as the oceanic component today suggests that ocean uptake of $^{14}\text{CO}_2$ today is close to natural pre-bomb conditions. However, if we extrapolate the oceanic component of the global $\Delta^{14}\text{CO}_2$ trend to the future, it appears that the ocean will likely become a source of $^{14}\text{CO}_2$ to the atmosphere within the next decade, earlier than predicted by Caldeira et al. (1998).

4.3. Simulated components of the interhemispheric $\Delta^{14}\text{CO}_2$ difference

During the period of strong atmospheric nuclear bomb tests, $\Delta^{14}\text{CO}_2$ in the northern troposphere exceeded that in the southern troposphere by up to 300‰ (compare Fig. 2) because the

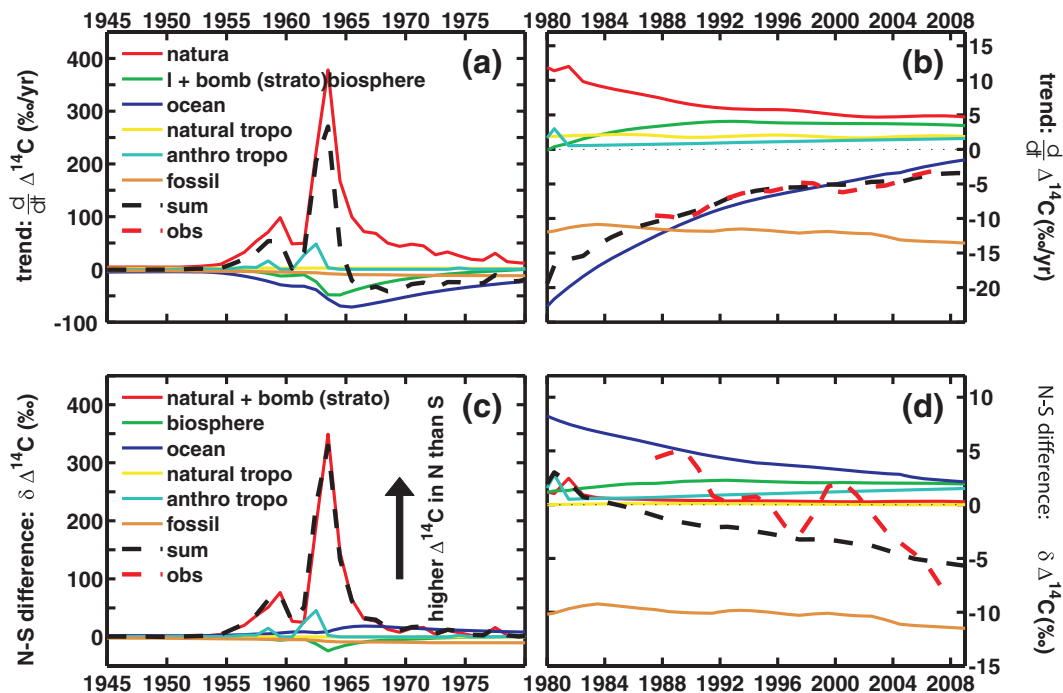


Fig. 7. Simulated components of the global tropospheric mean $\Delta^{14}\text{CO}_2$ trend (in ‰ per year, top panels, see Section 2.3.1. for details) and the tropospheric hemispheric mean north–south difference (in ‰, bottom panels, see Section 2.3.2. for details). The left panels depict the period 1945–1980, whereas the right panels show results for 1980–2009. Note that our approach does not distinguish between input of natural and bomb radiocarbon from the stratosphere into the troposphere. Also note that the anthropogenic ^{14}C component in the troposphere (light blue line) is dominated by tropospheric bomb radiocarbon input until the 1980s, but by radiocarbon emissions from the nuclear industry later on.

major part of the radiocarbon was produced in the northern hemisphere. Since oceanic uptake of excess radiocarbon occurred mainly in the southern ocean, this process increases the north–south $\Delta^{14}\text{CO}_2$ difference throughout the bomb era. Only uptake of excess radiocarbon by the biosphere, mainly operating in the northern hemisphere, can produce an opposite north–south difference until the biosphere turns from a sink of excess ^{14}C to a source in the 1980s (Naegler and Levin, 2009a), resulting in a change of sign of the biospheric contribution to the interhemispheric $\Delta^{14}\text{CO}_2$ difference at that time.

In the post-bomb era (i.e. since ca. 1980), the largest contribution to the north–south $\Delta^{14}\text{CO}_2$ difference stems from fossil fuel CO_2 emissions in the north, which are only partly compensated by the asymmetry of oceanic and biospheric $^{14}\text{CO}_2$ disequilibrium fluxes and higher $^{14}\text{CO}_2$ release into the northern troposphere by the nuclear industry (Fig. 7d). However, as the oceanic component of the interhemispheric $\Delta^{14}\text{CO}_2$ difference decreases

and since the biospheric release and anthropogenic ^{14}C production components are small, fossil CO_2 emissions remain the only ‘major’ driver of the north–south $\Delta^{14}\text{CO}_2$ difference today. The sum of all processes contributing to the simulated north–south $\Delta^{14}\text{CO}_2$ difference (dashed black line) does not exactly match the observed difference (dashed red line) which indicates either some missing processes, and/or incorrect boundary conditions in the model, or problems with data representativeness (compare discussion in Section 4.6).

4.4. Simulated components of the $\Delta^{14}\text{CO}_2$ seasonal cycle

As shown in Fig. 5, the GRACE model reproduces the mean seasonal cycle of $\Delta^{14}\text{CO}_2$ well at all stations for the last decade. The top row of Fig. 8 shows the components of the simulated $\Delta^{14}\text{CO}_2$ seasonal cycle in southern (left-hand side) and

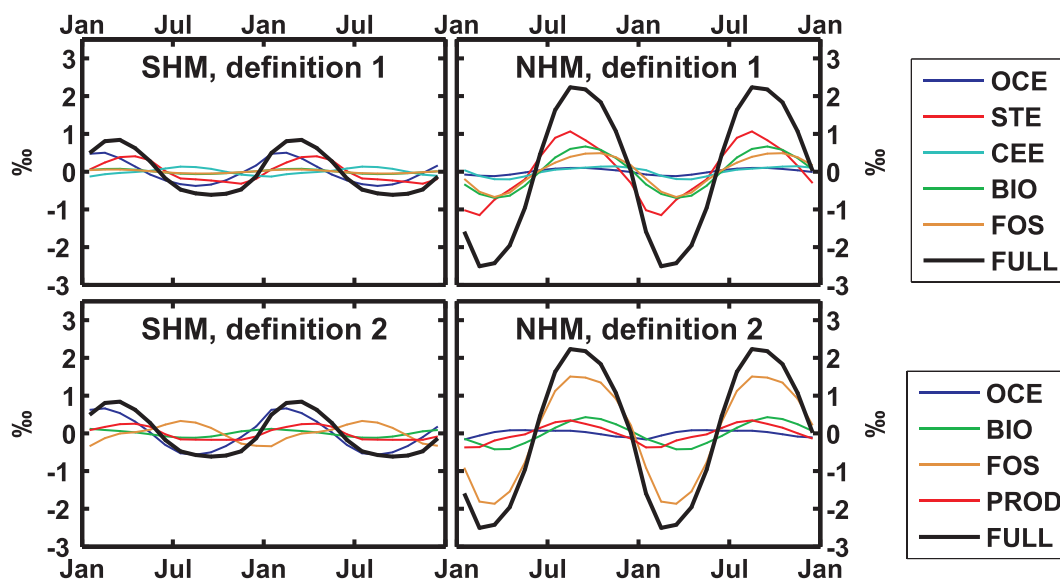


Fig. 8. Components of the simulated $\Delta^{14}\text{CO}_2$ seasonal cycle (2000–2001) calculated with both approaches defined in Section 2.3.3: In the top row, seasonal $\Delta^{14}\text{C}$ variability due to seasonally varying atmospheric mixing is regarded as an individual process (see Definition 1 in eq. 15), whereas in the bottom row, the contribution of seasonally varying mixing is broken down to the underlying source and sink processes (see Definition 2, eq. 18). ‘STE’ denotes stratosphere–troposphere exchange, ‘CEE’: cross-equator exchange, ‘BIO’ biospheric carbon fluxes, ‘FOS’ fossil fuel CO_2 emissions. ‘FULL’ is the sum of all components, i.e. the full seasonal cycle. ‘OCE’ refers to seasonal variability of oceanic carbon fluxes (due to variability of the piston velocity *and* the sea ice extent), ‘PROD’ is (stratospheric and tropospheric natural and anthropogenic) radiocarbon production.

northern (right-hand side) mid-latitudes for 2000–2001. In these figures, the contribution of each process (source, sink, atmospheric transport) to the $\Delta^{14}\text{CO}_2$ seasonal cycle has been calculated as the difference between a standard simulation and a simulation where the seasonality of each process has been shut off (Definition 1, see Section 2.3.3, eq. 15). In both hemispheres, seasonally varying STE of air (and tracer) contributes significantly to the seasonal $\Delta^{14}\text{CO}_2$ cycle (red line). Note, however, that $\pm 40\%$ weaker STE in the southern hemisphere (see Supplementary Information) results in a smaller STE component of the $\Delta^{14}\text{C}$ seasonal cycle in the south. Therefore, in the southern hemisphere, the amplitude of the oceanic contribution is of similar magnitude to that of STE. In the northern hemisphere, the sum of the seasonal contributions from carbon exchange with the biosphere (assimilation and heterotrophic respiration) and fossil fuel CO_2 emissions are of similar magnitude as the seasonal effect of STE alone.

As mentioned above in Section 2.3.3 (Definition 2, see eq. 18), seasonally varying transport – that is, STE and CEE – contributes to the $\Delta^{14}\text{C}$ seasonal cycle *only* because source and sink processes (such as oceanic or biospheric carbon fluxes, fossil fuel CO_2 release or – natural and anthropogenic – radiocarbon production) cause $\Delta^{14}\text{C}$ differences between both hemispheres (relevant for CEE), respectively, between stratosphere and troposphere (relevant for STE). Thus, the contributions of seasonally varying STE (red line in Fig. 8, top panels) and CEE (light blue line) to the seasonal tropospheric $\Delta^{14}\text{C}$ variability may further

be split into these source and sink components, if the contribution of each source and sink to the north–south respectively stratosphere–troposphere $\Delta^{14}\text{C}$ difference are known. Components of the interhemispheric $\Delta^{14}\text{CO}_2$ exchange have already been shown in Figs. 7c and d. In a similar manner, components of the vertical $\Delta^{14}\text{C}$ difference between lower stratosphere and troposphere can be calculated. In the south, the vertical $\Delta^{14}\text{C}$ difference is dominated by stratospheric ^{14}C production and oceanic uptake of ^{14}C (not shown). In contrast, in the north, it is controlled by natural ^{14}C production, but also by the northern tropospheric $\Delta^{14}\text{C}$ ‘sink’ due to release of ^{14}C -free fossil fuel CO_2 (also not shown).

The components to the $\Delta^{14}\text{C}$ seasonal cycle resulting from Definition 2 are shown in the lower panels of Fig. 8: Due to the strong horizontal and vertical $\Delta^{14}\text{CO}_2$ gradients imposed by fossil fuel CO_2 input in the northern troposphere, in this definition the northern hemispheric $\Delta^{14}\text{C}$ seasonal cycle is dominated by the fossil fuel component, whereas the overall $^{14}\text{CO}_2$ production term (natural and industrial) and the biosphere component are small. The ocean contributes very little to the seasonal $\Delta^{14}\text{CO}_2$ signal in the north. In the southern hemisphere, next to the oceanic component, the fossil fuel component becomes a major contribution to the seasonal $\Delta^{14}\text{CO}_2$ cycle. Based on these results, we conclude that the $\Delta^{14}\text{CO}_2$ seasonality today is dominated by respective temporal atmospheric transport patterns, which exert a seasonal signal on $\Delta^{14}\text{CO}_2$ mainly because of the large spatial gradients caused by fossil fuel combustion.

4.5. Simulated interannual variations of $\Delta^{14}\text{CO}_2$

Numerous processes contributing to the global carbon cycle (like air–sea gas exchange, mixing within the ocean and the atmosphere, respectively, biospheric assimilation and heterotrophic respiration, biomass burning) are subject to considerable interannual variability, leaving an imprint not only on the atmospheric CO_2 mixing ratio, but also on the $\delta^{13}\text{C}$ and $\Delta^{14}\text{C}$ signature of atmospheric CO_2 (Keeling et al., 2005; 2008; Allison et al., 2009) (compare Fig. 6). In the standard set up of GRACE, atmospheric mixing, air–sea gas exchange, NPP and heterotrophic respiration are not subject to interannual variability, resulting e.g. in the much smoother decrease of the simulated north–south $\Delta^{14}\text{C}$ difference compared to the observations (Fig. 6i). However, to estimate the sensitivity of atmospheric $\Delta^{14}\text{CO}_2$ to the variability of individual processes and to allow drawing conclusions about the variability of the global carbon cycle itself, we performed a number of sensitivity studies with the GRACE model. We distinguished two cases: (1) Variability on a time scale of 5 yr, which is a typical period of large-scale climatic variability like ENSO, and (2) a year-to-year variability. In the case of (1), we increased the respective parameter (e.g. atmosphere–ocean gas exchange rate) in the first 2.5 yr of each half decade by 20% and decreased the parameter in the second 2.5 yr by 20% (both deviations with respect to its standard value). In the case of the year-to-year variability, we multiplied the parameter in question with a 1σ function which varied randomly from year to year, and which had an average of 1 and a SD of $\pm 20\%$.

In general, the sensitivity of atmospheric $\Delta^{14}\text{CO}_2$ on the variability of STE, air–sea gas exchange, and heterotrophic respiration depends on the $\Delta^{14}\text{CO}_2$ gradients between stratosphere and troposphere, between troposphere and sea-surface, and between troposphere and terrestrial biosphere, respectively. Therefore, the simulated sensitivity is generally largest in the 1960s and 1970s, when the global radiocarbon cycle was strongly out of equilibrium due to the input of bomb-produced radiocarbon into the system. In recent years, however, the radiocarbon gradients between the main carbon reservoirs became relatively small, and the most sensitive processes for short-term $\Delta^{14}\text{CO}_2$ changes are STE and exchange between the atmosphere and the terrestrial biosphere. However, no single process alone is capable of producing atmospheric $\Delta^{14}\text{CO}_2$ excursions of more than $1\text{--}2\text{‰}$ from our climatological standard run, neither on the half-decadal nor on the annual time scale (not shown). This particularly means that the origin of the large interannual variation of the meridional gradient observed in the second half of the 1980s and around 2000 (see Fig. 4f) has not yet been univocally identified. One should also keep in mind that the measurement uncertainty of $\pm 2\text{--}3\text{‰}$ of individual data may result in an ‘artificial’ variability of the (fitted) long-term trend, which is hard to distinguish from ‘real’ interannual variability. Thus we cannot exclude at this time that part of the interannual variability, for example, of

the $\Delta^{14}\text{CO}_2$ differences from the Neumayer fit curve seen in Fig. 4f is not due to an analytical artefact.

4.6. Discrepancy between simulated and observed north–south difference in tropospheric $\Delta^{14}\text{C}$

Interestingly though, GRACE simulated a $\Delta^{14}\text{C}$ difference between northern and southern mid latitudes that is on average $3 \pm 2\text{‰}$ lower than the observations (i.e. too low $\Delta^{14}\text{C}$ in the northern or too high $\Delta^{14}\text{C}$ in the southern hemisphere), albeit with a decreasing trend (see Fig. 7d). This discrepancy might be explained by two different assumptions:

(1) The north–south distribution of ^{14}C sources and sinks in GRACE might not be realistic, that is, we are missing $\Delta^{14}\text{CO}_2$ sources in the north and/or $\Delta^{14}\text{CO}_2$ sinks in the south. To test this assumption, we conducted a number of sensitivity runs where we (i) shifted the median of the zonal mean NPP distribution towards the north by ca. 5° , (ii) changed $\Delta^{14}\text{C}$ values in the surface ocean by $+15\text{‰}$ in the north and by -15‰ in the circum-Antarctic ocean after the WOCE survey (and interpolating this adjustment linearly between the Arctic and Antarctica), (iii) changed the parametrization of the gas exchange coefficient k from quadratic to cubic, which increases the disequilibrium flux in particular in the southern ocean where wind speed is high, (iv) decreased global fossil fuel CO_2 emissions by 5% and (v) increased industrial ^{14}C production (occurring only in the north) by a factor of two. The last two cases would also change the long-term trend of tropospheric $\Delta^{14}\text{C}$. Only in the case where we assumed higher radiocarbon emissions from the nuclear industry the north–south $\Delta^{14}\text{C}$ difference is changed by up to $+2\text{‰}$. If we apply a cubic relationship between wind speed and piston velocity or if we adjust sea surface $\Delta^{14}\text{C}$ as described above, the north–south $\Delta^{14}\text{C}$ difference increased by ca. $+1\text{‰}$ relative to our standard run. Changes in the NPP distribution or fossil fuel emissions had a minimal effect on the simulated gradients ($+0.5\text{‰}$ or less).

(2) The mismatch between simulated and observed NHM–SHP difference in tropospheric $\Delta^{14}\text{C}$ could also be explained if the $\Delta^{14}\text{CO}_2$ observations at Jungfraujoch and Neumayer were not representative for the large NHM respectively SHP boxes in GRACE. It has been previously shown by 3D atmospheric transport model simulations using the LMDZ model (Turnbull et al., 2009) that Jungfraujoch observations are probably influenced by regional fossil CO_2 emissions from the European continent. Also, comparison of $\Delta^{14}\text{CO}_2$ at Jungfraujoch with Mace Head shows a small depletion of $1.0 \pm 0.5\text{‰}$ at Jungfraujoch (Section 3.2). However, a respective ‘adjustment’ of the Jungfraujoch observations to higher values would only produce a larger model–data mismatch. Concerning the representativeness of the Neumayer (and also Macquarie Island) observations, these may indeed be slightly lower than the mean $\Delta^{14}\text{CO}_2$ level between 30°S and 90°S to be compared with the GRACE model

results. But comparison with the LMDZ model results (Turnbull et al., 2009) shows that not more than 1‰ could be explained by this effect. Furthermore, due to the coarse vertical resolution, GRACE is not capable of simulating vertical $\Delta^{14}\text{C}$ gradients within the planetary boundary layer, which may contribute to the difference between GRACE and the observations, although this uncertainty is hard to quantify. Finally, a comparison of the interhemispheric exchange time τ with independent estimates (see Section S2.5.) indicates that τ might be uncertain by up to 25%, resulting in uncertainties of the simulated north–south differences of similar magnitude.

4.7. Comparison with results from Randerson et al. (2002)

Randerson et al. (2002) is the only published study which used a global 3-D transport model (with a horizontal resolution of $8^\circ \times 10^\circ$ and 9 vertical levels) to simulate atmospheric $\Delta^{14}\text{CO}_2$ from 1955 to 2000. This work focused on the seasonal and latitudinal variability of tropospheric $\Delta^{14}\text{CO}_2$, but did not present a full time series of absolute tropospheric $\Delta^{14}\text{CO}_2$, which then could be compared with observations. Furthermore, they do not present simulated time series of the atmospheric CO_2 mixing ratio or its $\delta^{13}\text{C}$. The $\Delta^{14}\text{CO}_2$ difference between 47°N (Jungfraujoch) and 71°S (Neumayer) simulated by Randerson et al. (2002) is shown as the blue line in Fig. 6i. For the overlapping period until 1990, their results agree with the GRACE simulation results and thus, also underestimate the observed north–south difference by a few permil.

Randerson et al. (2002) simulate a seasonal $\Delta^{14}\text{CO}_2$ (peak-to-trough) amplitude of ca.11‰ for high northern latitudes (Fruholmen) in the late 1980s, which is in agreement with observations from Fruholmen (71°N , Norway) from Nydal and Lövseth (1996). In contrast, GRACE simulates a $\Delta^{14}\text{C}$ seasonal amplitude for the NHP box at that time of 6‰, which is approximately 1‰ lower than our observations from Alert (82°N , amplitude ca. 7‰) in the late 1980s. The uncertainty of the individual $\Delta^{14}\text{C}$ measurements from Nydal and Lövseth (1996) is on the order of $\pm 10\%$, while the uncertainty of the $\Delta^{14}\text{C}$ measurements presented here is $\pm 2\text{--}4\%$. Thus, the seasonal amplitude in the Fruholmen data is not well defined due to larger measurement errors. Consequently, Randerson et al. (2002) might overestimate the seasonal amplitude of tropospheric $\Delta^{14}\text{CO}_2$. In their simulations, the seasonal cycle is dominated by the injection of radiocarbon from the stratosphere and by fossil fuel emissions, whereas the effect of the biosphere and the ocean is negligible during the late 1980s. In contrast, in our simulations, the major driver of the tropospheric $\Delta^{14}\text{CO}_2$ seasonal cycle in the northern hemisphere in the late 1980s is the low $\Delta^{14}\text{C}$ in the northern troposphere due to fossil fuel CO_2 emissions and the resulting interhemispheric and cross-tropopause $\Delta^{14}\text{C}$ differences in combination with seasonally varying STE and CEE. Natural

radiocarbon production as well as the oceans and the biosphere contribute roughly equally to the northern $\Delta^{14}\text{C}$ seasonality in the 1980s. Their combined effect is of similar magnitude as the fossil fuel component alone (not shown). In the southern hemisphere in the late 1980s – similar as today – seasonal $\Delta^{14}\text{CO}_2$ variations are hardly visible in the data (e.g. Fig. 4 right column). Therefore, we refrain here from comparing our model results with those of Randerson et al. (2002).

4.8. Stability of the fossil fuel component of the $\Delta^{14}\text{C}$ trend and north–south difference

Despite an increase in the fossil-fuel CO_2 emissions of more than 50% since the 1980s (Marland et al., 2007), the fossil fuel component of the $\Delta^{14}\text{C}$ trend and north–south difference stayed nearly unchanged in the last three decades (Figs. 7b and d). This was already pointed out by Randerson et al. (2002). Qualitatively, this surprising stability can easily be understood: The isotopic difference between the atmosphere and fossil fuels has decreased rapidly, as bomb ^{14}C was taken up by the oceans (and biosphere) and atmospheric $\Delta^{14}\text{C}$ decreased rapidly since the (tropospheric mean) maximum in 1965 (see Fig. 2). This decrease in the disequilibrium happens to have been roughly balanced by the increase in the fossil fuel flux, resulting in a roughly constant net effect of fossil fuel CO_2 on $\Delta^{14}\text{CO}_2$. Quantitatively, this can be calculated as follows: The fossil fuel component of the global $\Delta^{14}\text{C}$ trend (see eq. 6) is

$$\begin{aligned} \left(\frac{d}{dt}\Delta^{14}\text{C}\right)_{\text{FF}} &= C p_{\text{FF, norm}} \\ &= f \left[\frac{1}{n^{\text{C}}} \cdot \left(\frac{dn^{14}}{dt}\right)_{\text{FF}} - \frac{n^{14}}{(n^{\text{C}})^2} \cdot \left(\frac{dn^{\text{C}}}{dt}\right)_{\text{FF}} \right] \\ &= -f \frac{n^{14}}{n^{\text{C}}} \frac{1}{n^{\text{C}}} \left(\frac{dn^{\text{C}}}{dt}\right)_{\text{FF}} \\ &= -f R^{14} \frac{1}{n^{\text{C}}} \left(\frac{dn^{\text{C}}}{dt}\right)_{\text{FF}} \\ &= -f R^{14} F_{\text{FF, norm}}^{\text{C}} \\ \text{with } F_{\text{FF, norm}}^{\text{C}} &= \frac{1}{n^{\text{C}}} \left(\frac{dn^{\text{C}}}{dt}\right)_{\text{FF}}, \end{aligned} \quad (20)$$

note that $\frac{d}{dt}n_{\text{FF}}^{14} = 0$ and $n^{14}/n^{\text{C}} = R^{14}$. This finding is illustrated in Fig. 9.

A similar reasoning holds for the fossil fuel component of the interhemispheric $\Delta^{14}\text{C}$ difference: As the major part of fossil CO_2 emissions occurs in the northern hemisphere, $\delta\Delta^{14}\text{C}_{\text{FF}}$ can be approximated by $-(f R^{14} \frac{1}{n^{\text{C}}} \frac{d}{dt}n_{\text{FF}}^{\text{C}})_{\text{NH}}$. Here again, the decrease of R^{14} nearly compensates the increase in $\frac{d}{dt}n_{\text{FF}}^{\text{C}}/n^{\text{C}}$, resulting in a nearly constant $\delta\Delta^{14}\text{C}_{\text{FF}}$.

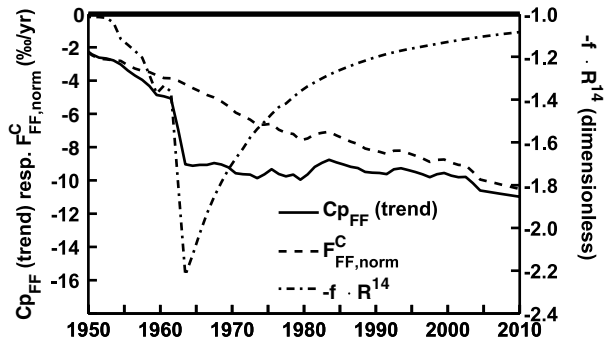


Fig. 9. Total fossil fuel component $C_{p_{FF}}^C$ of the global $\Delta^{14}C$ trend, which is almost constant since the mid 1960s, and the two factors contributing to this component (see eq. 20).

4.9. Estimates of uncertainties of the component analysis of GRACE simulations and its constraints on global fossil fuel CO_2 emissions

Today, fossil fuel CO_2 emissions F_{FF}^C are the major drivers of both the north–south difference and the global $\Delta^{14}C$ trend (see Figs. 7b and d). Thus, in principle, both the observed N–S difference in atmospheric $\Delta^{14}C$ and the trend could be used as independent constraints for reported fossil fuel emissions. However, the combined uncertainty of all other components of the N–S difference is ca. 3.0‰ (Table 3), which is on the order of 25% of the fossil fuel CO_2 component contributing to the $\Delta^{14}C$ difference between north and south. Together with an additional uncertainty of 25% in the interhemispheric exchange time τ used to calculate the components of the N–S difference (see eq. 12f), the total uncertainty of the fossil-fuel derived CO_2 emissions estimated from the observed N–S difference of atmospheric $\Delta^{14}C$ is on the order of ca. 30% (see Table 3). Similarly, if fossil fuel CO_2 emissions F_{FF}^C are estimated from the observed global $\Delta^{14}C$

trend, the combined uncertainties in the biospheric and oceanic contribution as well as the natural and industrial production result in an overall uncertainty of F_{FF}^C of ca. 25%. Thus neither the observed north–south difference in atmospheric $\Delta^{14}CO_2$ nor the observed global $\Delta^{14}CO_2$ trend impose strong constraints on global fossil CO_2 emissions.

5. Conclusions and perspectives

Dedicated deployment of our global carbon (isotope) model GRACE for the period 1940 till today revealed that recent figures of global carbon dioxide exchange fluxes between atmosphere, ocean and biosphere are largely in accordance with the observed global distribution and trends of $\Delta^{14}CO_2$ in the atmosphere. By this attempt, it was possible to model observed temporal trends of atmospheric CO_2 , $\delta^{13}CO_2$ and $\Delta^{14}CO_2$ from pre-bomb times through the bomb era up until the most recent time, where the global $^{14}CO_2$ cycle is mainly disturbed by fossil fuel CO_2 emissions. The major processes contributing to the observed changes in atmospheric $\Delta^{14}CO_2$ could be quantitatively determined with the GRACE model, leading to the following implications: The ocean–atmosphere disequilibrium today is close to pre-industrial times, but, due to increasing fossil fuel CO_2 emissions, the ocean will most probably be turning from a sink of radiocarbon (natural but also anthropogenic) to a source over the next decade. This is considerably earlier than predicted by Caldeira et al. (1998).

Deploying the current global source/sink distribution of CO_2 in combination with adjusted atmospheric transport parameters implemented in the GRACE model, we were also able to quantitatively reproduce the observed seasonal cycles of $\Delta^{14}CO_2$ at background stations, both in the northern and southern hemispheres, and to determine the components contributing to the seasonality. While in the 1960s the seasonality was driven by spatial and interreservoir gradients of bomb ^{14}C , today it is

Table 3. Factors contributing to the uncertainty of the tropospheric $\Delta^{14}C$ trend ($\frac{d}{dt}\Delta^{14}C$) and the north–south difference ($\delta\Delta^{14}C$) in 2008

Unit	Uncertainty $\frac{d}{dt}\Delta^{14}C$ (‰/a)	Uncertainty $\delta\Delta^{14}C$ (due to τ) (‰)	Uncertainty $\delta\Delta^{14}C$ (due to fluxes) (‰)	Total uncertainty $\delta\Delta^{14}C$ (‰)
^{14}C input from stratosphere	1.0	0.1	0.1	0.1
Biosphere	1.7	0.5	1.0	1.1
Ocean	2.3	0.5	2.4	2.5
Natural ^{14}C troposphere	0.6	0.0	0.0	0.0
Anthrop. ^{14}C troposphere	1.6	0.4	1.5	1.6
Fossil CO_2 emissions	0.7	2.9	0.6	3.0
Total non-fossil- CO_2	3.5	0.8	3.0	3.1

Note: Both uncertainties in the interhemispheric exchange time τ of 25% (column 3) as well as uncertainties in the total strength and spatial distribution of CO_2 and ^{14}C fluxes (column 4) contribute to the total uncertainty of $\delta\Delta^{14}C$ (column 5).

mainly controlled by gradients due to fossil fuel emissions. These are modulated by the seasonal variability of atmospheric transport taking into account both, interhemispheric and STE.

However, we are still not capable of quantitatively explaining the north–south gradient of $\Delta^{14}\text{CO}_2$ which since the 1980s is lower by $3 \pm 2\%$ in the model compared to observations, although this discrepancy seems to be decreasing in the last few years. It may be possible that our observational sites are not fully representative for the large box size in the GRACE model; still, other models with higher spatial resolution such as Randerson et al. (2002) and Turnbull et al. (2009) have also observed similar deficits in simulating the north–south gradient. More recent measurements of $\Delta^{14}\text{C}$ in surface ocean water dissolved inorganic carbon as well as a better understanding of the dependency of the gas exchange coefficient k on wind velocity would improve the knowledge on the oceanic component of the north–south gradient. Also a re-assessment of ^{14}C sources from civil and military nuclear facilities (mainly in the north) would help to reduce the uncertainty in the simulated north–south gradient. However, significantly higher ^{14}C emissions from nuclear facilities needed to reconcile model and observations would require a fundamental re-assessment of the global radiocarbon budget.

Constraining carbon cycle dynamics in the future with observations of atmospheric $\Delta^{14}\text{C}$ would require extremely high precision and accuracy as well as a significant expansion of the existing network towards $\Delta^{14}\text{C}$ observations close to the relevant source and sink regions. For example, estimating the regional fossil fuel CO_2 component of Europe (Levin et al., 2003; Levin and Karstens, 2007), or North America (Turnbull et al., 2006; Graven et al., 2009) has been shown to be feasible with high-precision $^{14}\text{CO}_2$ observations. In this context, improved simulation of atmospheric transport in high-resolution models (Levin and Rödenbeck, 2008) as well as observation-based regional estimates of the ^{14}C -disequilibrium between atmosphere and biosphere are indispensable. Over the ocean, in addition to long-term, regionally resolved monitoring, also surface ocean water $\Delta^{14}\text{C}$ measurements to determine the ocean–atmosphere $\Delta^{14}\text{C}$ disequilibrium are needed for a quantitative understanding of (radio-) carbon cycle dynamics. As long as these technical and infrastructural obstacles are not overcome, high precision atmospheric $\Delta^{14}\text{C}$ measurements at a few representative stations in the northern, southern and equatorial regions are still extremely valuable to provide the necessary input function for future applications of ^{14}C as a (dating) tracer of atmospheric, terrestrial or oceanic carbon pools.

6. Acknowledgments

This work would not have been possible without the dedicated efforts and long-term support by the staff at the sampling sites, at Neumayer, Macquarie Island, Cape Grim, Mérida Observatory, Izaña, Jungfraujoch, Mace Head and Alert, as well as the technical personnel, in particular Sabine Kühr, in the Heidel-

berg Radiocarbon Laboratory. The authors wish to thank Vago Hesshaimer, who developed the first version of the GRACE model, Andreas Schäfer who helped with the model transport optimization, Felix Vogel for technical support with the Figures as well as Philippe Ciais, and Matthias Cuntz for many helpful suggestions and discussions. Special thanks are also to the two anonymous reviewers for their detailed comments, which helped to improve the manuscript. This long-term work was partly funded by a number of agencies in Germany and Europe, namely the Heidelberg Academy of Sciences, the Ministry of Education and Science, Baden-Württemberg, Germany; the German Science Foundation, the German Minister of Environment; the German Minister of Science and Technology; the German Umweltbundesamt and the European Commission, Brussels, as well as national funding agencies in Australia, Canada and Spain.

References

- Andres, R.J., Marland, G. and Bischof, S. 1996. Global and latitudinal estimates of ^{13}C from fossil fuel consumption and cement manufacture, ORNL/CDIAC, Oak Ridge Natl. Lab. Report db1013, Oak Ridge, Tenn. USA.
- Allison, C.E., Francey, R.J. and Krummel, P.B. 2009. $\delta^{13}\text{C}$ in CO_2 from sites in the CSIRO Atmospheric Research GASLAB air sampling network, (2009 version). In: *Trends: A Compendium of Data on Global Change, Carbon Dioxide Information Analysis Center*, Oak Ridge National Laboratory, U.S. Department of Energy, Oak Ridge, TN, USA.
- Battle, M., Bender, M.L., Tans, P.P., White, J.W.C., Ellis, J.T. and co-authors. 2000. Global carbon sinks and their variability inferred from atmospheric O_2 and $\delta^{13}\text{C}$. *Science* **287**, 2467–2470.
- Bousquet, P., Peylin, P., Ciais, P., Le Quééré, C., Friedlingstein, P. and co-authors. 2000. Regional changes in carbon dioxide fluxes of land and oceans since 1980. *Science* **290**, 1342–1346.
- Braziunas, T.F., Fung, I.Y. and Stuiver, M. 1995. The preindustrial atmospheric $^{14}\text{CO}_2$ latitudinal gradient as related to exchanges among atmospheric, oceanic, and terrestrial reservoirs. *Global Biogeochem. Cycles* **9**(4), 565–584.
- Broecker W.S. and Peng, T.-H. 1994. Stratospheric contribution to the global bomb radiocarbon inventory: model versus observations. *Global Biogeochem. Cycles* **8**, 377–384.
- Broecker W.S., Peng, T.-H., Östlund, G. and Stuiver, M. 1985. The distribution of bomb radiocarbon in the ocean. *J. Geophys. Res.* **90**(C4), 6953–6970.
- Caldeira, K., Rau, G.H. and Duffy, P.B. 1998. Predicted net efflux of radiocarbon from the ocean and increase in atmospheric radiocarbon content. *Geophys. Res. Lett.* **25**(20), 3811–3814.
- Ciais, P., Tans, P.P., Trolier, M., White, J.W.C. and Francey, R.J. 1995. A large Northern Hemisphere terrestrial CO_2 sink indicated by the $^{13}\text{C}/^{12}\text{C}$ ratio of atmospheric CO_2 . *Science* **269**, 1098–1102.
- Cox, P.M., Betts, R.A., Jones, C.D., Spall, S.A. and Totterdell, I.J. 2000. Acceleration of global warming due to carbon-cycle feedbacks in a coupled climate model. *Nature* **408**, 184–187.

- Cramer, W, Kicklighter, D.W., Bondeau, A., Moore, B., III, Churkina, G. and co-authors. 1999. Comparing global models of terrestrial net primary productivity (NPP): overview and key results. *Global Change Biol.* **5**(suppl. 1), 1–15.
- Czeplak, G. and Junge, C. 1974. Studies of interhemispheric exchange in the troposphere by a diffusion model. *Adv. Geophys.* **18**, 57–72.
- Damon, P.E. and Sternberg, R.E. 1989. Global production and decay of radiocarbon. *Radiocarbon* **31**, 697–703.
- Degens, E.T. 1969. Biogeochemistry of stable carbon isotopes. In: *Organic Geochemistry: Methods and Results*, (eds G. Eglinton and M.T. Murphy). Springer, Berlin, Germany, 304–439.
- Denman, K.L., Brasseur, G., Chidthaisong, A., Ciais, P., Cox, P.M. and co-authors. 2007. Couplings Between Changes in the Climate System and Biogeochemistry. In: *Climate Change 2007: The Physical Science Basis. Contribution of Working Group I to the Fourth Assessment Report of the Intergovernmental Panel on Climate Change* (eds S. Solomon, D. Qin, M. Manning, Z. Chen, M. Marquis, K.B. Averyt, M. Tignor and H.L. Miller). Cambridge University Press, Cambridge, United Kingdom and New York, NY, USA.
- Dörr, H. and Münnich, K.O. 1986. Annual variations of the ^{14}C content of soil CO_2 . *Radiocarbon* **28**(2A), 338–345.
- Duffy, P.B., Eliason, D.E., Bourgeois, A.J. and Covey, C.C. 1995. Simulation of bomb radiocarbon in two global general circulation models. *J. Geophys. Res.* **100** (C11), 22545–22563.
- Enting, I.G. 1982. *Nuclear Weapons Data for Use in Carbon Cycle Modeling*, Commonwe. Sci. and Ind. Res. Organ., Melbourne, Australia, 1–18, pp.
- Francey, R.J., Tans, P.P., Allison, C.E., Enting, I.G., White, J.W.C. and co-authors. 1995. Changes in oceanic and terrestrial carbon uptake since 1982. *Nature* **373**, 326–330.
- Francey, R.J., Allison, C.E., Etheridge, D.M., Trudinger, C.M., Enting, I.G. and co-authors. 1999. 1000-year high precision record of $\delta^{13}\text{C}$ in atmospheric CO_2 . *Tellus* **51B**, 170–190.
- Friedli, H., Loetscher, H., Oeschger, H., Siegenthaler, U. and Stauffer, B. 1986. Ice core record of the $^{13}\text{C}/^{12}\text{C}$ ratio of atmospheric carbon dioxide in the past two centuries. *Nature* **324**, 237–238.
- Friedlingstein, P., Dufresne, J.-L., Cox, P.M. and Rayner, P. 2003. How positive is the feedback between the climate change and the carbon cycle? *Tellus* **55B**, 692–700.
- Gaudinski, J.B., Trumbore, S.E., Davidson, E.A. and Zheng, S.H. 2000. Soil carbon cycling in a temperate forest: radiocarbon-based estimates of residence times, sequestration rates and partitioning of fluxes. *Biogeochemistry* **51**(1), 33–69.
- GlobalView-CO2, Cooperative Atmospheric Data Integration Project – Carbon Dioxide, *Tech. rep.*, NOAA ESRL, Boulder, CO, USA, 2008, available via anonymous FTP: ftp.cmdl.noaa.gov, path: ccg/CO2/GLOBALVIEW.
- Goudriaan, J. 1992. Biosphere structure, carbon sequestration potential and the atmospheric ^{14}C carbon record. *J. Exp. Bot.* **43**, 1111–1119.
- Gibson, J.K., Kållberg, P., Uppala, S., Hernandez, A., Nomura, A. and co-authors. 1997. CMWF Re-Analysis, Project Report Series: 1. ERA description, European Center for Mid-Range Weather Forecast, Reading, UK.
- Graven, H.D., Stephens, B.B., Guilderson, T.P., Campos, T.L., Schimel, D.S. and co-authors. 2009. Vertical profiles of biospheric and fossil fuel-derived CO_2 and fossil fuel CO_2 : CO ratios from airborne measurements of $\Delta^{14}\text{C}$, CO_2 and CO above Colorado, USA. *Tellus* **61B**, doi:10.1111/j.1600-0889.2009.00421.x.
- Gurney, K.R., Law, R.M., Denning, A.S., Rayner, P.J., Baker, D. and co-authors. 2002. Toward robust regional estimates of CO_2 sources and sinks using atmospheric transport models. *Nature* **415**, 626–630.
- Hesshaimer, V., Heimann, M. and Levin, I. 1994. Radiocarbon evidence for a smaller oceanic carbon dioxide sink than previously believed. *Nature* **370**, 201–203.
- Houghton, R.A. 2003. Revised estimates of the annual net flux of carbon to the atmosphere from changes in land use and land management 1850–2000. *Tellus* **55B**, 378–390.
- Hua, Q. and Barbetti, M. 2004. Review of tropospheric bomb ^{14}C data for carbon cycle modelling and age calibration purposes. *Radiocarbon* **46**, 1–26.
- Jacob, D.J., Prather, M.J., Wofsy, S.C. and McElroy, M.B. 1987. Atmospheric distribution of ^{85}Kr simulated with a general circulation model. *J. Geophys. Res.* **92**, 6614–6626.
- Jain, A.K., Kheshgi, H.S. and Wuebbles, D.J. 1996. A globally aggregated reconstruction of cycles of carbon and its isotopes. *Tellus* **48B**, 583–600.
- Johnston, H.S. 1989. Evaluation of excess carbon-14 and strontium-90 data for suitability to test two-dimensional stratospheric models. *J. Geophys. Res.* **94**, 18485–18493.
- Joos, F. and Bruno, M. 1998. Long-term variability of the terrestrial and oceanic carbon sinks and the budgets of the carbon isotopes ^{13}C and ^{14}C . *Global Biogeochem. Cycles* **12**(2), 277–295.
- Kalnay, E., Kanamitsu, M., Kistler, R., Collins, W., Deaven, D. and co-authors. 1996. The NCEP/NCAR 40-year reanalysis project. *Bull. Am. Meteorol. Soc.* **77**, 437–471.
- Keeling, C.D., Whorf, T.P., Wahlen, M. and Van Der Plicht, J. 1995. Interannual extremes in the rate of rise of atmospheric carbon dioxide since 1980. *Nature* **375**, 666–670.
- Keeling, C.D., Bollenbacher, A.F. and Whorf, T.P. 2005. Monthly atmospheric $^{13}\text{C}/^{12}\text{C}$ isotopic ratios for 10 SIO stations. In: *Trends: A Compendium of Data on Global Change*. Carbon Dioxide Information Analysis Center, Oak Ridge National Laboratory, Oak Ridge, Tenn., USA.
- Keeling, R.F., Piper, S.C., Bollenbacher, A.F. and Walker, J.S. 2008. Atmospheric CO_2 records from sites in the SIO air sampling network. In: *Trends: A Compendium of Data on Global Change*. Carbon Dioxide Information Analysis Center, Oak Ridge National Laboratory, U.S. Department of Energy, Oak Ridge, Tenn., USA.
- Key, R.M., Kozyr, A., Sabine, C.L., Lee, K., Wanninkhof, R. and co-authors. 2004. A global ocean carbon climatology: results from Global Data Analysis Project (GLODAP). *Global Biogeochem. Cycles* **18**(4), GB4031, doi:10.1029/2004GB002247.
- Kjellström, E., Feichter, J. and Hoffmann, G. 2000. Transport of SF_6 and $^{14}\text{CO}_2$ in the atmospheric general circulation model ECHAM. *Tellus* **52B**, 1–18.
- Krakauer, N.Y., Randerson, J.T., Primeau, F.W., Gruber, N. and Mendenlis, D. 2006. Carbon isotope evidence for the latitudinal distribution and wind speed dependence of the air-sea gas transfer velocity. *Tellus* **58B**, 390–417.
- Kromer B. and Münnich, K.O. 1992. CO_2 gas proportional counting in Radiocarbon dating—review and perspective. In: *Radiocarbon After*

- Four Decades* (eds R. E. Taylor, A. Long and R. S. Kra). Springer-Verlag, New York, 184–197.
- Land, C., Feichter, J. and Sausen, R. 2002. Impact of vertical resolution on the transport of passive tracers in the ECHAM4 model. *Tellus* **54B**, 344–360.
- Lassey, K.R., Enting, I. and Trudinger, C.M. 1996. The earth's radiocarbon budget: a consistent model of the global carbon and radiocarbon cycles. *Tellus* **48B**, 487–501.
- Le Quéré, C., Aumont, O., Bopp, L., Bousquet, P., Ciais, P. and co-authors. 2003. Two decades of ocean CO_2 sink and variability. *Tellus* **55B**, 649–656.
- Levin, I., Münnich, K.O. and Weiss, W. 1980. The effect of anthropogenic CO_2 and ^{14}C sources on the distribution of $^{14}\text{CO}_2$ in the atmosphere. *Radiocarbon* **22**, 379–391.
- Levin, I., Kromer, B., Schoch-Fischer, H., Bruns, M., Münnich, M. and co-authors. 1985. 25 Years of tropospheric ^{14}C observations in Central Europe. *Radiocarbon* **27**, 1–19.
- Levin, I., Kromer, B., Wagenbach, D. and Münnich, K.O. 1987. Carbon isotope measurements of atmospheric CO_2 at a coastal station in Antarctica. *Tellus* **39B**, 89–95.
- Levin, I., Börsinger, R., Bonani, G., Francey, R.J., Kromer, B. and co-authors. 1992. Radiocarbon in atmospheric carbon dioxide and methane: global distribution and trends. In: *Radiocarbon After Four Decades: An Interdisciplinary Perspective* (eds R. E. Taylor, A. Long and R.S. Kra). Springer-Verlag, New York, 503–517.
- Levin, I. and Heshshaimer, V. 1996. Refining of atmospheric transport model entries by the globally observed passive tracer distributions of $^{85}\text{krypton}$ and sulfur hexafluoride (SF_6). *J. Geophys. Res.* **101**, 16745–16755.
- Levin, I. and Heshshaimer, V. 2000. Radiocarbon—a unique tracer of global carbon cycle dynamics. *Radiocarbon* **42**, 69–80.
- Levin, I. and Kromer, B. 1997. Twenty years of atmospheric $^{14}\text{CO}_2$ observations at Schauinsland station, Germany. *Radiocarbon* **39**, 205–218.
- Levin, I., Kromer, B., Schmidt, M. and Sartorius, H. 2003. A novel approach for independent budgeting of fossil fuel CO_2 over Europe by $^{14}\text{CO}_2$ observations. *Geophys. Res. Lett.* **30**(23), 2194 doi:10.1029/2003GL018477.
- Levin, I. and Kromer, B. 2004. The tropospheric $^{14}\text{CO}_2$ level in mid-latitudes of the Northern Hemisphere (1959–2003). *Radiocarbon* **46**(3), 1261–1272.
- Levin, I. and Karstens, U. 2007. Inferring high-resolution fossil CO_2 records at continental sites from combined $^{14}\text{CO}_2$ and CO observations. *Tellus* **59B** (2), 245–250.
- Levin, I. and Rödenbeck, C. 2008. Can the envisaged reductions of fossil fuel CO_2 emissions be detected by atmospheric observations? *Naturwissenschaften* **95**, 206–208.
- Levin, I., Hammer, S., Kromer, B. and Meinhardt, F. 2008. Radiocarbon observations in atmospheric CO_2 : determining fossil fuel CO_2 over Europe using Jungfraujoch observations as background. *Sci. Total Environ.*, **391**, 211–216.
- Levitus, S., Boyer, T., Conkright, M., O'Brien, T., Antonov, J. and co-authors. 1998. *World Ocean Database 1998*. National Oceanic and Atmospheric Administration, Silver Spring, MD, USA.
- Libby, W.F. 1961. Radiocarbon dating (Noble Lecture). *Science* **133**, 621–629.
- Lingenfelter, R.E. 1963. Production of carbon 14 by cosmic-ray neutrons. *Rev. Geophys.* **1**, 35–55.
- Maier-Reimer, E. and Hasselmann, K. 1987. Transport and storage of CO_2 in the ocean—an inorganic ocean-circulation carbon cycle model. *Clim. Dyn.* **2**, 63–90.
- Manning, M.R., Lowe, D.C., Melhuish, W.H., Sparks, R.J., Wallace, G. and co-authors. 1990. The use of radiocarbon measurements in atmospheric studies. *Radiocarbon* **32**(1), 37–58.
- Manning, A.C. and Keeling, R.F. 2006. Global oceanic and land biotic carbon sinks from the Scripps atmospheric oxygen flask sampling network. *Tellus* **58B**(2), 95–116.
- Manning, M.R. and Melhuish, W.H. 1994. Atmospheric ^{14}C record from Wellington. In: *Trends: A Compendium of Data on Global Change, Carbon Dioxide Information Analysis Center, Oak Ridge, TN, USA*.
- Marland, G., Boden, T.A. and Andres, R.J. 2007. Global, Regional, and National Fossil Fuel CO_2 Emissions. In: *Trends: A Compendium of Data on Global Change, Carbon Dioxide Information Analysis Center, Oak Ridge National Laboratory, U.S. Department of Energy, Oak Ridge, Tenn., USA*.
- McCormac, F.G., Reimer, P.J., Hogg, A.G., Higham, T.F.G., Baillie, M. and co-authors. 2002. Calibration of the radiocarbon time scale for the southern hemisphere: AD 1850–950. *Radiocarbon* **44**(3), 641–651.
- Meijer, H.A.J., Van Der Plicht, J., Gislefoss, J.S. and Nydal, R. 1995. Comparing long-term atmospheric ^{14}C and ^3H records near Groningen, The Netherlands with Fruholmen, Norway and Izaña, Canary Islands ^{14}C stations. *Radiocarbon* **37**(1), 39–50.
- Meijer, H.A.J., Pertuisot, M.H. and Van Der Plicht, J. 2006. High-accuracy ^{14}C measurements for atmospheric CO_2 samples by AMS. *Radiocarbon* **48**(3), 355–372.
- Morimoto, S., Nakazawa, T., Higuchi, K. and Aoki, S. 2000. Latitudinal distribution of atmospheric CO_2 sources and sinks inferred by $\delta^{13}\text{C}$ measurements from 1985 to 1991. *J. Geophys. Res.* **105** (D19), 24315–24326.
- Müller, S.A., Joos, F., Plattner, G.-K., Edwards, N.R. and Stocker, T.F. 2008. Modelled natural and excess radiocarbon—sensitivities to the gas exchange formulation and ocean transport strength. *Global Biogeochem. Cycl.* **22**, GB3011, doi:10.1029/2007GB003065.
- Naegler, T., Ciais, P., Rodgers, K. and Levin, I. 2006. Excess radiocarbon constraints on air-sea gas exchange and the uptake of CO_2 by the oceans. *Geophys. Res. Lett.* **33**, L11802, doi:10.1029/2005GL025408.
- Naegler, T. and Levin, I. 2006. Closing the global radiocarbon budget 1945–2005. *J. Geophys. Res.* **111**, D12311, doi:10.1029/2005JD006758.
- Naegler, T. 2009. Reconciliation of excess ^{14}C -based global CO_2 piston velocity estimates. *Tellus* **61B**, 372–384, doi:10.1111/j.1600-0889.2008.00408.x.
- Naegler, T. and Levin, I. 2009a. Observation-based global biospheric excess radiocarbon inventory 1963–2005. *J. Geophys. Res.* **114**, D17302, doi:10.1029/2008JD011100.
- Naegler, T. and Levin, I. 2009b. Biosphere-atmosphere gross carbon exchange flux and the $\delta^{13}\text{C}$ and $\Delta^{14}\text{C}$ disequilibria constrained by the biospheric excess radiocarbon inventory. *J. Geophys. Res.* **114**, D17303, doi:10.1029/2008JD011116.
- Nakazawa, T., Ishizawa, M., Higuchi, K. and Trivett, N.B.A. 1997. Two curve fitting methods applied to CO_2 flask data. *Environmetrics* **8**, 197–218.

- Nydal, R. and Lövseth, K. 1983. Tracing bomb ^{14}C in the atmosphere 1962–1980. *J. Geophys. Res.* **88**, 3621–3642.
- Nydal, R. and Lövseth, K. 1996. Carbon-14 measurements in atmospheric CO_2 from northern and southern hemisphere sites, 1962–1993. ORNL/CDIAC-93, NDP-057, Oak Ridge National Laboratory, Oak Ridge, TN, USA.
- Oeschger, H., Siegenthaler, U., Schotterer, U. and Gugelmann, A. 1975. A box diffusion model to study the carbon dioxide exchange in nature. *Tellus* **27**(2), 168–192.
- Piper, S.C., Keeling, C.D. and Stewart, E.F. 2001. Exchange of atmospheric CO_2 and ^{13}C with the terrestrial biosphere and the oceans from 1978 to 2001. II. A three-dimensional tracer inversion model to deduce regional fluxes. SIO Reference Series. Scripps Institution of Oceanography, La Jolla, CA, USA.
- Prentice, I.C., Farquhar, G.D., Fasham, M.J.R., Goulden, M.L., Heimann, M. and co-authors. 2001. The carbon cycle and atmospheric CO_2 . In: *Climate Change: The scientific basis, the contribution of WGI of the IPCC to the IPCC Third Assessment Report (TAR)* (eds J. T. Houghton, Y. Ding, D. J. Griggs, M. Noguer, P. J. van der Linden and co-editors). Cambridge University Press, Cambridge, UK.
- Quay, P., Sonnerup, R., Westby, T., Stutsman, J. and McNichol, A. 2003. Changes in the $^{13}\text{C}/^{12}\text{C}$ of dissolved inorganic carbon in the ocean as a tracer of anthropogenic CO_2 uptake. *Global Biogeochem. Cycles* **17**(1), 1004, doi:10.1029/2001GB001817.
- Randerson, J.T., Enting, I.G., Schuur, E.A.G., Caldeira, K. and Fung, I.Y. 2002. Seasonal and latitudinal variability of troposphere $\Delta^{14}\text{CO}_2$: post bomb contributions from fossil fuels, oceans, the stratosphere, and the terrestrial biosphere. *Global Biogeochem. Cycles* **16**(4), 1112, doi:10.1029/2002GB001876.
- Rayner, P.J., Enting, I.G., Francey, R.J. and Langenfelds, R. 1999. Reconstructing the recent carbon cycle from atmospheric CO_2 , $\delta^{13}\text{C}$ and O_2/N_2 observations. *Tellus* **51B**, 213–232.
- Rayner, P.J., Law, R.M., Allison, C.E., Francey, R.J., Trudinger, C.M. and co-authors. 2008. The interannual variability of the global carbon cycle (1992–2005) inferred by inversion of atmospheric CO_2 and ^{13}C measurements. *Global Biogeochem. Cycles* **22**, GB3008, doi:10.1029/2007GB003068.
- Reimer, P.J., Baillie, M.G.L., Bard, E., Bayliss, A., Beck, J.W. and co-authors. 2004. INTCAL04 terrestrial radiocarbon age calibration, 0–26 cal kyr BP. *Radiocarbon* **46**(3), 1029–1058.
- Rödenbeck, C., Houweling, S., Gloor, M. and Heimann, M. 2003. Time-dependent atmospheric CO_2 inversions based on interannually varying tracer transport. *Tellus* **55B**, 488–497.
- Rodgers, K.B., Cane, M.A. and Schrag, D.P. 1997. Seasonal variability of sea surface $\Delta^{14}\text{C}$ in the equatorial Pacific in an ocean circulation model. *J. Geophys. Res.* **102** (C8), 18627–18638.
- Rozanski, K., Levin, I., Stock, J., Guevara Falcon, R.E. and Rubio, F. 1995. Atmospheric $^{14}\text{CO}_2$ variations in the equatorial region. *Radiocarbon* **37**, 509–515.
- Sabine, C.L., Feely, R.A., Gruber, N., Key, R.M., Lee, K. and co-authors. 2004. The oceanic sink for anthropogenic CO_2 . *Science* **305**, 367–371.
- Siegenthaler, U., Heimann, M. and Oeschger, H. 1980. ^{14}C variations caused by changes in the global carbon cycle. *Radiocarbon* **22**, 177–191.
- Siegenthaler, U. and Joos, F. 1992. Use of a simple model for studying oceanic tracer distributions and the global carbon cycle. *Tellus* **44B**, 186–207.
- Stuiver, M. and Polach, H. 1977. Discussion: reporting of ^{14}C data. *Radiocarbon* **19**, 355–363.
- Stuiver, M. and Quay, P. 1981. Atmospheric ^{14}C changes resulting from fossil fuel CO_2 release and cosmic ray flux variability. *Earth Planet. Sci. Lett.* **53**, 349–362.
- Stuiver, M. and Reimer, P. 1993. Extended ^{14}C data base and revised CALIB 3.0 ^{14}C Age calibration program. *Radiocarbon* **35**, 215–230.
- Stuiver, M. and Braziunas, T.F. 1998. Anthropogenic and Solar Components of Hemispheric ^{14}C . *Geophys. Res. Lett.* **25**(3), 329–332.
- Suess, H.E. 1955. Radiocarbon concentration in modern wood. *Science* **122**, 415.
- Sweeney, C., Gloor, M., Jacobson, A.R., Key, R.M., McKinley, G. and co-authors. 2007. Constraining air-sea gas exchange for CO_2 with recent bomb ^{14}C measurements. *Global Biogeochem. Cycles* **21**, GB2015, doi:10.1029/2006GB002784.
- Telegadas, K. 1971. The seasonal atmospheric distribution and inventories of excess carbon-14 from March 1955 to July 1969. HASL report 243, Health and Safety Lab., U.S. At. Energy Comm., New York.
- Toggweiler, J.R., Dixon, K. and Bryan, K. 1989. Simulations of radiocarbon in a coarse-resolution world ocean model 1: steady state prebomb distributions. *J. Geophys. Res.* **94**, 8217–8242.
- Turnbull, J., Miller, J.B., Lehman, S.J., Tans, P.P., Sparks, R.J. and Southon, J. 2006. Comparison of $^{14}\text{CO}_2$, CO , and SF_6 as tracers for recently added fossil fuel CO_2 in the atmosphere and implications for biological CO_2 exchange. *Geophys. Res. Lett.* **33**, L01817, doi:10.1029/2005GL024213.
- Turnbull, J., Rayner, P., Miller, J.B., Naegler, T., Ciais, P. and Cozic, A. 2009. On the use of $^{14}\text{CO}_2$ as a tracer for fossil fuel CO_2 : quantifying uncertainties using an atmospheric transport model. *J. Geophys. Res.* doi:10.1029/2009JD011982.
- Trumbore, S.E. 1993. Comparison of carbon dynamics in tropical and temperate soils using radiocarbon measurements. *Global Biogeochem. Cycles* **7**(2), 275–290.
- Trumbore, S.E. 2000. Age of soil organic matter and soil respiration: radiocarbon constraints on belowground C dynamics. *Ecol. Appl.* **10**(2), 399–411.
- Trumbore, S.E. 2009. Radiocarbon and soil carbon dynamics. *Annu. Rev. Earth Planet. Sci.* **37**, 47–66.
- UNSCEAR. 2000. Sources and effects of ionizing radiation, UNSCEAR 2000 Report to the General Assembly, United Nations Scientific Committee on the Effects of Atomic Radiation, Vienna, Austria.
- Vogel, J.C., Fuls, A., Visser, E. and Becker, B. 1993. Pretoria calibration curve for short-lived samples, 1930–3350 BC. *Radiocarbon* **35**, 73–85.
- Vogel, J.C., Fuls, A. and Visser, E. 2002. Accurate dating with radiocarbon from the atom bomb tests. *S. Afric. J. Sci.* **98**, 437–438.
- Wanninkhof, R. 1992. Relationship between wind speed and gas-exchange over the ocean. *J. Geophys. Res.* **97**(C5), 7373–7382.
- Yang, X., North, R. and Romney, C. 2000. CMR nuclear explosion database (revision 3), CMR Tech. Rep. 00/16, Cent. for Monitor. Res., U. S. Army Space and Missile Defense Command, Arlington, VA.